

# ADVANCED MATERIALS

## Supporting Information

for *Adv. Mater.*, DOI: 10.1002/adma.201806931

Assembling 2D MXenes into Highly Stable Pseudocapacitive  
Electrodes with High Power and Energy Densities

*Armin VahidMohammadi, Mehrnaz Mojtavavi, Nuala Mai  
Caffrey, Meni Wanunu, and Majid Beidaghi\**

## Supporting Information

### **Assembling 2D MXenes into Highly Stable Pseudocapacitive Electrodes with High Power and Energy Densities**

Armin VahidMohammadi, Mehrnaz Mojtavavi, Nuala Mai Caffrey, Meni Wanunu, and Majid Beidaghi\*

A. VahidMohammadi, Prof. M. Beidaghi  
Department of Mechanical and Material Engineering, Auburn University, Auburn, AL 36849, USA.  
E-mail: [mbeidaghi@auburn.edu](mailto:mbeidaghi@auburn.edu)

M. Mojtavavi, Prof. M. Wanunu  
Department of Bioengineering, Northeastern University, Boston, Massachusetts 02115, USA.

Prof. M. Wanunu  
Department of Physics, Northeastern University, Boston, Massachusetts 02115, USA.

Dr. N.M. Caffrey  
School of Physics and CRANN, Trinity College, Dublin 2, Ireland.

## Experimental Section

**Synthesis of MAX phases.**  $V_2AlC$  MAX phase was synthesized according to previous reports.<sup>[1]</sup> First, elemental powders of vanadium (99.5%, 325 mesh, Alfa Aesar), aluminum (99.5%, 325 mesh, Alfa Aesar), and graphite (99%, 325 mesh, Alfa Aesar) were mixed in a 2:1.3:1 molar ratio. After 18h of ball milling (using zirconia balls), the mixture was sintered under flowing argon atmosphere at 1500 °C for 4h with a heating rate of 3 °C min<sup>-1</sup>.  $Ti_2AlC$  MAX phase was prepared by mixing titanium carbide (99.5%, ~ 2 microns, Alfa Aesar), titanium (99.5%, 325 mesh, Alfa Aesar), and aluminum powders in a 0.85:1.15:1.05 molar ratio. The mixture was then ball milled for 24 h followed by sintering at 1400 °C for 4 h with a heating rate of 5 °C min<sup>-1</sup>. All synthesized MAX phases were milled using titanium carbide milling tips and sieved through a 400 mesh to obtain uniform powders with an average particle size of less than ~32 microns.

**Synthesis of multilayered MXenes.** Multilayered (ML)- $V_2CT_x$  MXenes were synthesized by immersing  $V_2AlC$  MAX phase in a 50% hydrofluoric acid solution (HF, ACS grade, BDH) in a ratio of 2 g powder to 40 mL etchant (schematic illustration of the synthesis process is shown in **Figure S1**). The mixture was stirred at 400 rpm for 92 h at room temperature using a Teflon coated magnetic bar. When etching was complete, the acid-treated powder was washed several times by DI water and the washing process was repeated until the pH of the supernatant was around 5. The produced ML- $V_2CT_x$  MXene powder was then filtered on a porous membrane, rinsed with DI water and collected from the filter membrane. Synthesis of ML- $Ti_2CT_x$  MXene was carried out as follows: First, an etching mixture was prepared by dissolving 2 g of LiF (98.5%, Alfa Aesar) in 40 mL 6 M HCl (ACS grade, BDH). The mixture was stirred for about 10 minutes to dissolve LiF completely. Then, 2 g of  $Ti_2AlC$  MAX phase was slowly (over 10 minutes) added to the etching solution which was placed in an ice bath. The etching was carried out for 24 h at 35 °C while stirring the mixture at 550 rpm. After etching, the produced powders were washed and filtered to collect the final ML- $Ti_2CT_x$ . Both MXene powders were dried under vacuum at room temperature for 12 h before any further processing or analysis.

**Delamination of MXenes.** The multilayered ML- $V_2CT_x$  and ML- $Ti_2CT_x$  MXenes were delaminated to single/few-layer sheets by treating them with tetra n-butyl ammonium hydroxide (TBAOH, 40 % w/w aqueous solution in water, Alfa Aesar). To intercalate MXenes with  $TBA^+$  cations, the produced multilayered powders were stirred in a TBAOH solution at 1000 rpm in a ratio of 200 mg MXene powder to 4 mL of TBAOH solution. The

process was carried at room temperature for 4 h for  $V_2CT_x$  and 2h for  $Ti_2CT_x$ . The pre-intercalated powders were then dispersed in 45 mL of DI water and transferred to centrifuge tubes. The dispersions were shaken by hand for 2 minutes and subsequently centrifuged for 10 minutes at 2,000 rpm. For the case of  $V_2CT_x$  powder, the supernatant obtained after the first round of shaking and centrifugation processes contained low concentrations (light green color) as well as residual TBAOH. Therefore, it was not used in our further studies. The delamination process was continued by adding DI water to the precipitate powder and repeating the shaking and centrifugation steps. The subsequent supernatants were collected (referred to as d- $V_2CT_x$  and d- $Ti_2CT_x$  solutions in the text) and used in further studies. The final product of the delamination process was dispersion of MXene flakes in water in concentrations ranging from 0.5 to 1 mg mL<sup>-1</sup>. The concentration of dispersions could be significantly increased by using sonication in the delamination process. However, due to the unstable nature of the d- $V_2CT_x$  and d- $Ti_2CT_x$  flakes, sonication will increase the oxidation rate of the flakes due to exposure to air and heat. Therefore, sonication was avoided in the delamination process.

**Cation-driven assembly of MXenes and fabrication of freestanding films.** To assemble delaminated MXene sheets, saturated aqueous solutions of LiCl (anhydrous, 99%, Alfa Aesar), NaCl (99%, Alfa Aesar),  $MgCl_2$  (anhydrous, 99%, Alfa Aesar), and  $Mg(ClO_4)_2$  (anhydrous, ACS grade, Alfa Aesar) were first prepared in such a way that the total mass of the salt in the solutions was at least 100 times higher than the mass of MXenes in their dispersions. The saturated salt solutions were then added slowly to the delaminated MXene solutions at room temperature. Upon addition of the salt solutions, the MXene flakes gradually assembled and precipitated at the bottom of the container (Figure S2). The solutions containing the assembled MXene flakes were slowly stirred, sealed, and kept for 30 min to allow all the assembled MXene flakes to precipitate. Then the clear supernatant was decanted and the assembled MXenes flakes were washed two times with DI water to remove any residual salt. After washing, 30 mL of water was added to the MXene flakes and the solution was slowly shaken by hand for 1 minute to get a uniform dispersion of restacked flakes. These dispersions were filtered on Celgard membranes to obtain freestanding MXene films. It is worth mentioning that for the MXenes assembled with  $Li^+$  cations, strong shaking resulted in partial disassembly and redispersion of assembled flakes in water. Therefore, strong shaking was avoided to prevent disassembly of the MXenes flakes. The freestanding MXene films were labeled as C- $V_2CT_x$ , where C is the cation used in the assembly process ( $Li^+$ ,  $Na^+$ , or  $Mg^{2+}$ ). In addition, freestanding films of delaminated MXenes without assembly (d- $V_2CT_x$

and d-Ti<sub>2</sub>CT<sub>x</sub>) were fabricated by directly filtering their corresponding dispersion on filter membranes.

**Electrochemical measurements.** All electrochemical measurements were carried out in plastic Swagelok cells where glassy carbon electrodes were used as current collectors for the working and counter electrodes. Ag wire coated with AgCl immersed in 1 M KCl was used as the reference electrode for all the tests. Working electrodes (WE) were prepared by directly punching the freestanding MXene films into the desired size. A piece of over-capacitive activated carbon film (YP-50) was used as the counter electrode (CE) in the cells. This electrode was prepared by first rolling a slurry of 95 wt.% activated carbon and 5 wt.% PTFE into freestanding films and punched to the required size. Their size, and mass, as controlled to be much higher than the working electrode. Aqueous solutions of 5 M LiCl, 1 M Li<sub>2</sub>SO<sub>4</sub>, 1 M Na<sub>2</sub>SO<sub>4</sub>, 1 M MgCl<sub>2</sub>, 1 M Mg<sub>2</sub>SO<sub>4</sub>, 1 M KOH, 0.5 M K<sub>2</sub>SO<sub>4</sub>, and 3 M H<sub>2</sub>SO<sub>4</sub> were used as electrolytes in the cells. All cells were initially stabilized by 50 charge and discharge cycles at a scan rate of 20 mV s<sup>-1</sup> prior to electrochemical measurements. CV experiments were done at scan rates ranging from 2 mV s<sup>-1</sup> to 10 Vs<sup>-1</sup>. The operating potential window of the MXene electrodes in each electrolyte was determined by using CV test cycling where the potential window was gradually increased until signs of electrolyte decomposition and/or MXene oxidation was observed. In all electrolytes, the upper cut-off potential was found to be the same as open circuit potential (OCP). The operating potential window in 5 M LiCl and 1 M Li<sub>2</sub>SO<sub>4</sub> electrolytes was set to be from 0 V to -1 V, in 1 M Na<sub>2</sub>SO<sub>4</sub>, 1 M MgSO<sub>4</sub>, 1 M MgCl<sub>2</sub>, and 0.5 M K<sub>2</sub>SO<sub>4</sub> it was set from 0 V to -0.8 V, and in 1 M KOH it was set between -0.6 and -1.2 V (All potential values vs Ag/AgCl). In 3 M H<sub>2</sub>SO<sub>4</sub> the upper cut-off potential was +0.2 V while the two lower cut-off potentials of -0.4 V and -0.6 V were studied. To evaluate the cycle life of the electrodes, galvanostatic charge/discharge experiments at current densities of 10 and 100 A g<sup>-1</sup> were carried out for 10,000 cycles in the corresponding potential window of each electrolyte.

Electrochemical impedance spectroscopy (EIS) data were collected in the same three-electrode setup, in the 100 mHz to 1,000 kHz frequency range. The EIS experiments were carried out at OCP and the applied potential amplitude was 10 mV. Symmetric supercapacitors were assembled by using V<sub>2</sub>CT<sub>x</sub> films (with equal weight) as both working and counter electrodes to evaluate the performance of fabricated V<sub>2</sub>CT<sub>x</sub> electrodes in full cells (two-electrode setup). The specific capacitance of each cell was calculated based on the total weight (or volume) of both MXene electrodes.

**Capacitance and rate-dependence charge storage mechanism calculations.** The capacitance of MXene electrodes was calculated from the reduction portion of the CV graphs at different scan rates by using the following equation:<sup>[2]</sup>

$$C = \frac{1}{\Delta V} \int \frac{j dV}{s} \quad (1)$$

where C is the normalized capacitance (F cm<sup>-3</sup> or F g<sup>-1</sup>), ΔV is the voltage window (V), j is the current density (mA cm<sup>-3</sup> or mA g<sup>-1</sup>), V is voltage (V), and s is the scan rate (mV s<sup>-1</sup>). The specific energy (E) and power (P) densities of the symmetric cells were calculated from CV graphs at different scan rates using the following equations:<sup>[3]</sup>

$$E = \left(\frac{1}{2} \times C \times V^2\right) / 3600 \quad [\text{Wh cm}^{-3}] \quad (1)$$

$$P = E \times \frac{s}{V} \times 3600 \quad [\text{W cm}^{-3}] \quad (2)$$

where C is the normalized capacitance of the cell (F cm<sup>-3</sup>), V is the cell operating potential window (V), and s is the scan rate (V/s).

The kinetics of the charge storage in the electrodes were evaluated at different scan rates by considering a power-law relationship between the current, i, and scan rate, ν (i=av<sup>b</sup>). A b value of 0.5 corresponds to a diffusion-controlled process and a b value of 1 represents a surface-controlled charge storage mechanism.<sup>[4]</sup> To distinguish these two processes, the total current value of each potential point was considered to have two different capacitive controlled and diffusion controlled contributions according to the following equation:<sup>[2]</sup>

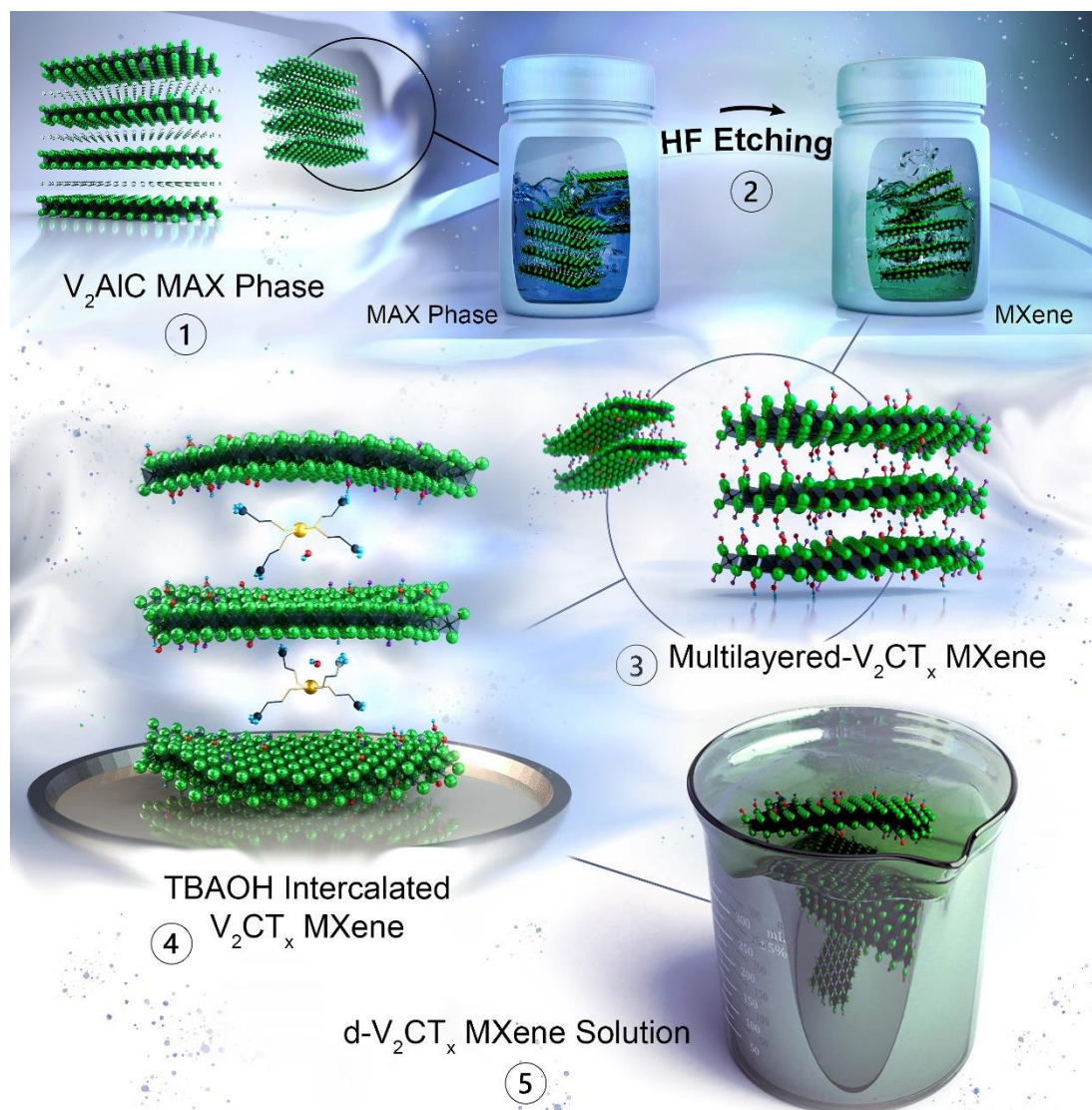
$$i(V) = k_1\nu + k_2\nu^{0.5} \quad (4)$$

where V is the potential and k<sub>1</sub> and k<sub>2</sub> are adjustable variables. k<sub>1</sub>ν determines capacitive contribution and k<sub>2</sub>ν<sup>0.5</sup> represents the diffusion-controlled contribution of the total charge stored.

**Characterization techniques.** XRD analyses of the samples were done directly on the fabricated freestanding films using Bruker X-ray diffractometer (D8 Discover) with 40 kV and 40 mA Cu-ka radiation at a scan speed of 0.2 seconds per 2θ step. For *ex situ* XRD analyses, the electrodes were pre-cycled at a scan rate of 20 mV s<sup>-1</sup>, and then cycled at 2 mV s<sup>-1</sup> and stopped at corresponding potentials. The cells were quickly opened and the electrodes were washed with DI water before analysis. For SEM analysis of the samples, a JEOL JSM-7000F scanning electron microscope equipped with an energy dispersive spectrometer (EDS detector) was used. A FEI Scios dual beam system with gallium ion beam source was used to prepare lamellae from cross-section of Na-V<sub>2</sub>CT<sub>x</sub>, Li-V<sub>2</sub>CT<sub>x</sub>, and d-V<sub>2</sub>CT<sub>x</sub> electrode films for

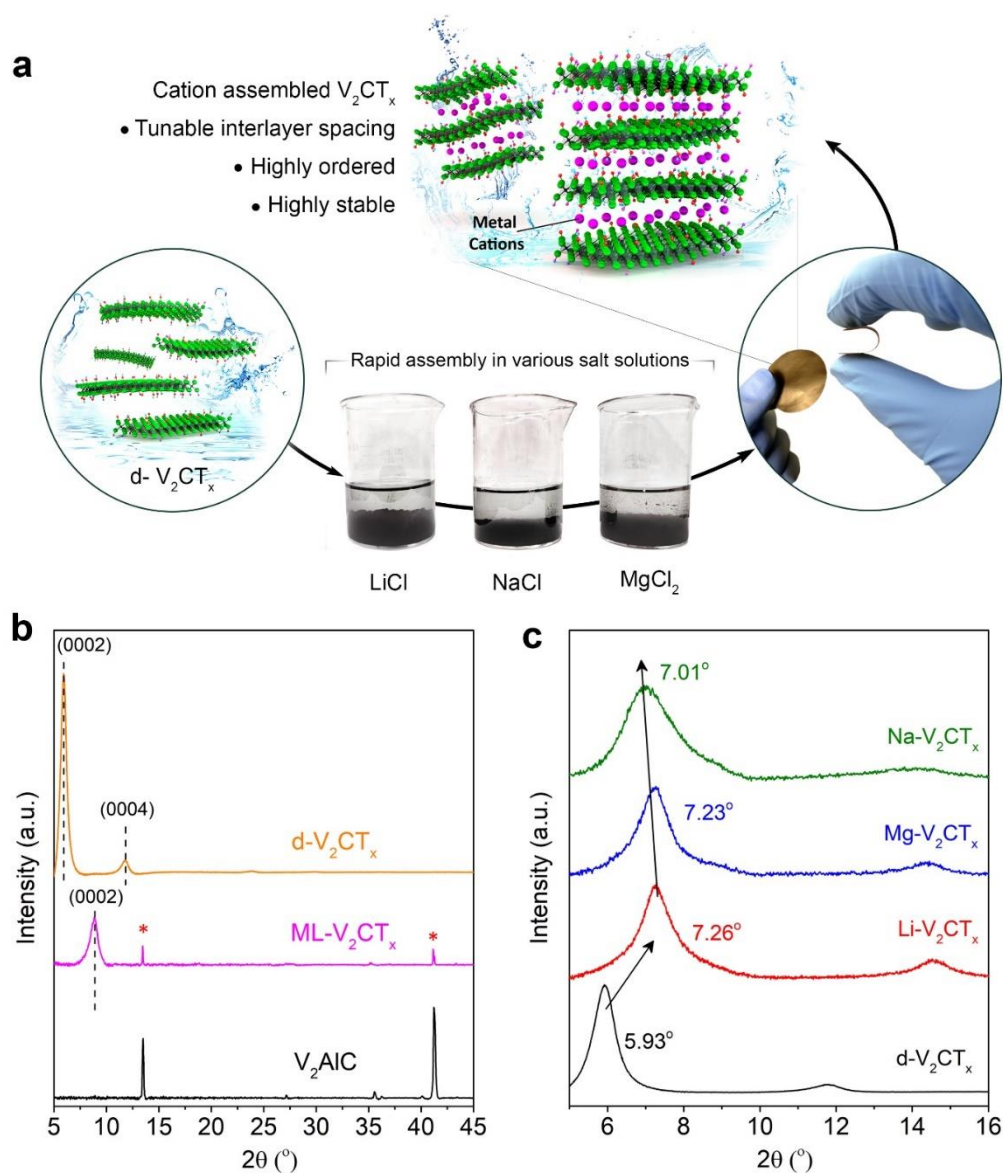
further characterization with electron microscopy. To prepare TEM samples, lamellas were thinned to a thickness of less than 100 nm and placed on a TEM grid. Some TEM samples were also prepared by drop casting the redispersed assembled  $V_2CT_x$  flakes on TEM grids. A probe-corrected FEI Titan Themis 300 S/TEM with ChemisSTEM technology was employed for imaging lamellas in both HR-TEM and STEM imaging modes and studying samples' structures. Furthermore, EDS analysis was performed at 300 kV using a SuperX EDS system for elemental analysis of samples and confirming the presence of cations in between the  $V_2CT_x$  layers. A Kratos AXIS 165 surface analysis instrument with a 165-mm hemispherical analyzer (HAS) was used to carry out X-ray photoemission spectroscopy analysis on the samples. The XPS chamber was purged with nitrogen and XPS spectra were recorded in fixed analyzer transmission (FAT) mode at 12 mA and 15 kV by using a monochromatic aluminum source. The step size for all measurements was 0.05 eV with 500 ms dwell time. Ar sputtering was done at 4 kV for 10 minutes with a large spot size of  $\sim 2 \text{ mm}^2$ . The resolution of the XPS machine was measured from FWHM of the  $Ag3d_{5/2}$  peak to be 1.0 eV and the incidence of the X-ray beam had an angle of  $54.7^\circ$  relative to the specimen normal. To calibrate the XPS energy scale, the  $Ag3d_{5/2}$  line of clean silver was set to exactly 368.3 eV referenced to the Fermi level. Delaminated MXene solutions or cation-assembled MXene dispersions were drop-casted on  $SiO_2$  coated silicon wafers for atomic force microscopy (AFM) measurements. Prepared samples were characterized by Park Instruments NX10 AFM using a non-contact mode cantilever.

**Computational methods.** Density functional theory calculations were performed using the VASP code.<sup>[5-7]</sup> The Perdew-Burke-Ernzerhof (PBE)<sup>[8]</sup> functional was employed. The plane wave basis set was converged using a 500eV energy cutoff. Structural relaxations of the supercell were carried out using a  $3 \times 3 \times 2$  k-point Monkhorst-Pack mesh.<sup>[9]</sup> The electronic structure was then calculated using a  $9 \times 9 \times 4$  mesh. Dispersion forces were included using the semi-empirical approach of Grimme (DFT-D3).<sup>[10]</sup> The surface sites of a  $3 \times 3$   $V_2C$  supercell were covered with mixed  $-O$ , and  $-F$  groups placed directly above the V atom on the opposite surface. Calculations were carried out considering full coverage of MXene surfaces with functional groups (nominal stoichiometry formula of  $V_2CF_{0.88}O_{1.11}$ ). As the number of  $-OH$  groups on the surface is typically found to be reduced or even eliminated after alkali atom intercalation,<sup>[11-13]</sup> this termination type was not considered. Li atoms were intercalated at a concentration of  $Li_{0.22}-V_2CT_x$ , close to what was found experimentally. A full structural relaxation was performed. After Li intercalation the c lattice parameter increased by 1 Å (from 13.7 Å to 14.7 Å).



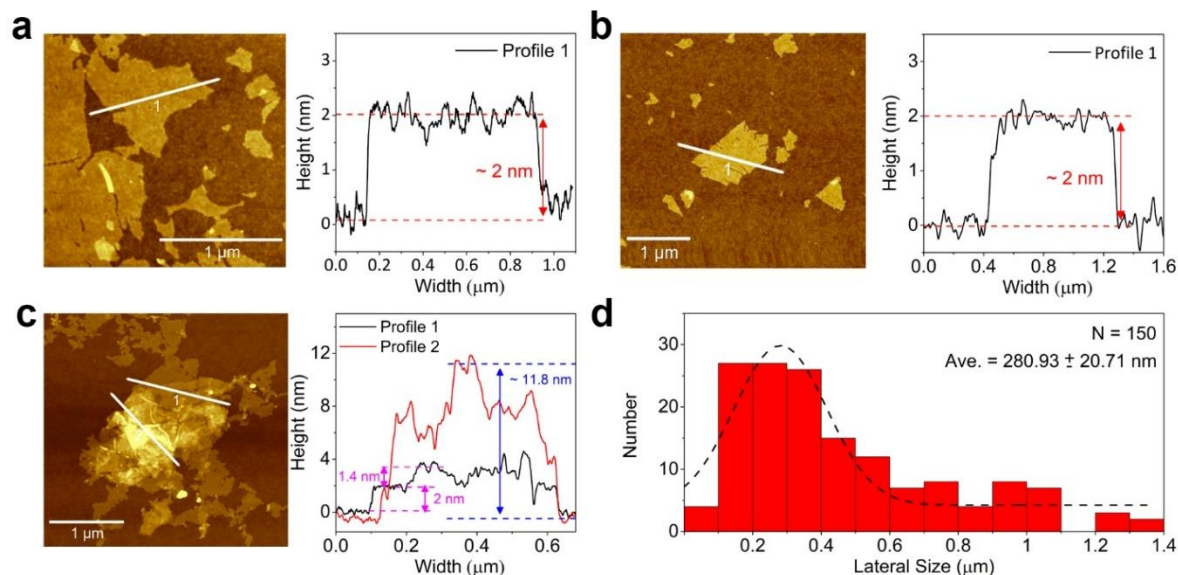
**Figure S1.** Schematic illustration of the synthesis and delamination of  $V_2CT_x$ . The synthesis method relies on expanding the interlayer spacing in the MAX phase in order to weaken interlayer interactions and facilitate delamination.<sup>[1,14,15]</sup> 1, Structure of  $V_2AlC$  MAX phase. 2, Selective etching of the  $V_2AlC$  in 50% HF solution for 92 h, where Al atoms are selectively etched. 3, Structure of the multilayered  $V_2CT_x$  (ML- $V_2CT_x$ ) showing the presence of different functional groups on the surface of the exfoliated MXene sheets. 4, Intercalation of tetrabutylammonium cations ( $TBA^+$ ) through treatment of the MXene powders in a solution of tetrabutylammonium hydroxide (TBAOH) at room temperature

resulting in expansion of interlayer spacing of ML- $V_2CT_x$ . As explained in Figure S2, XRD analysis showed an increase of about 4.93 Å in the interlayer spacing of the ML- $V_2CT_x$  after intercalation of  $TBA^+$  cations. 5, Delaminated  $V_2CT_x$  (d- $V_2CT_x$ ) solution obtained by hand shaking of the  $TBA^+$  intercalated ML- $V_2CT_x$  in water.



**Figure S2.** Assembly of  $V_2CT_x$  flakes and X-ray diffraction (XRD) characterization of fabricated M- $V_2CT_x$  films (M: Li, Na, Mg). (a) Schematic of  $d-V_2CT_x$  structure, digital photographs of the MXene dispersion after the addition of LiCl, NaCl, and  $MgCl_2$  solutions, digital photographs of the freestanding flexible films fabricated with vacuum filtration of the assembled MXene flakes, and schematic illustration of the assembled flakes. (b) XRD patterns of  $V_2AIC$  MAX phase, multilayered (ML)  $V_2CT_x$ , and delaminated  $V_2CT_x$  ( $d-V_2CT_x$ ). After HF treatment and selective removal of Al atoms, the intensities of the MAX phase peaks were significantly reduced and a new peak corresponding to (0002) plane of MXenes appeared at  $\sim 8.86^\circ$  (d-spacing: 9.97 Å, c-LP: 19.94 Å). After  $TBA^+$  intercalation and complete delamination of  $V_2CT_x$ , residual MAX phase powders were

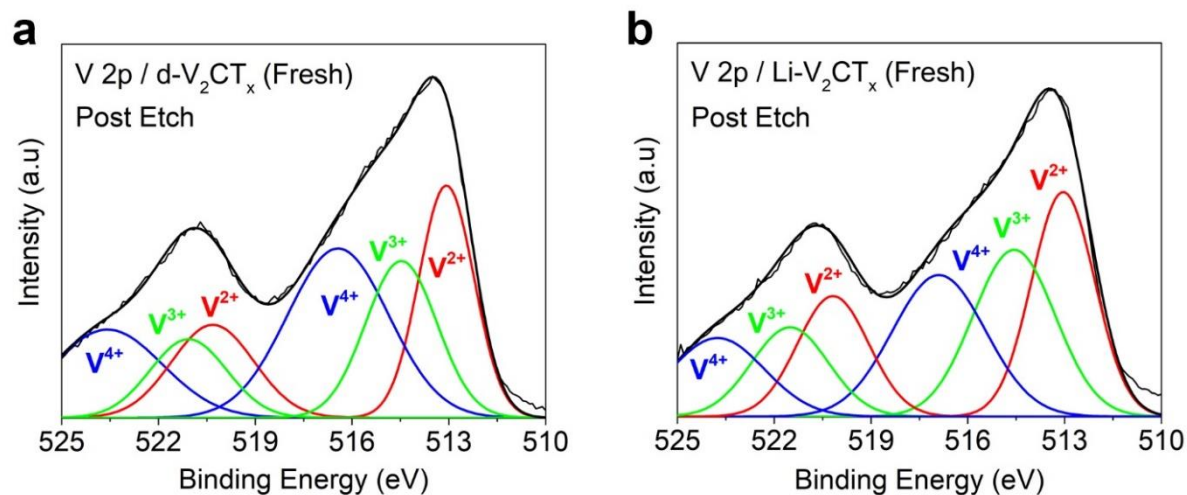
separated from delaminated MXene flakes by centrifugation. XRD pattern of the  $d\text{-V}_2\text{CT}_x$  films showed a large downshift in the (0002) peak position to  $5.93^\circ$  (d-spacing:  $14.89 \text{ \AA}$ , c-LP:  $29.78 \text{ \AA}$ ). Also, another peak corresponding to (0004) plane of MXene was appeared at  $\sim 11.75^\circ$ . (c) Enlarged portion of the XRD patterns of the films shown in Figure 2b of the article for low angles.



**Figure S3.** Atomic force microscopy (AFM) images of  $\text{V}_2\text{CT}_x$  MXene. (a and b) AFM images and corresponding height profiles of the delaminated  $\text{V}_2\text{CT}_x$  ( $d\text{-V}_2\text{CT}_x$ ) showing mostly single layer flakes in the delaminated solutions with an apparent thickness of  $\sim 2 \text{ nm}$ . The higher than theoretical thickness observed here is due to the interactions between the silicon substrate and different functional groups present on the surface of MXene flakes. Similar observations have been reported for AFM measurements of  $\text{Ti}_3\text{C}_2\text{T}_x$  flakes.<sup>[16,17]</sup> (c) AFM image of  $\text{Li-V}_2\text{CT}_x$  ( $\text{V}_2\text{CT}_x$  assembled with  $\text{Li}^+$ ) and the corresponding height profiles. Assembly of  $\text{V}_2\text{CT}_x$  flakes is evident in the AFM image. The thickness of  $\text{Li-V}_2\text{CT}_x$  flakes is around  $11.8 \text{ nm}$ , which corresponds to around 8 layers of MXene (thickness of first layer in contact with silicon wafer is around  $2 \text{ nm}$ , while AFM measurements on folded areas showed a thickness of  $\sim 1.4 \text{ nm}$  for single layer  $\text{V}_2\text{CT}_x$  on top of the first layer). (d) Average lateral size and size distribution of the synthesized  $\text{V}_2\text{CT}_x$  MXene flakes calculated by measuring the size of 150 individual flakes using AFM. The produced  $d\text{-V}_2\text{CT}_x$  solutions showed an average lateral flake size of  $280.93 \pm 20.71 \text{ nm}$ .

**Table S1.** Deconvolution results of XPS peaks for various samples in V 2p<sub>3/2</sub> region.

Vanadium Species	V <sup>2+</sup> (eV)	%	V <sup>3+</sup> (eV)	%	V <sup>4+</sup> (eV)	%	V <sup>5+</sup> (eV)	%
Fresh d-V <sub>2</sub> CT <sub>x</sub>	513.4	28%	514.76	5%	516.5	67%	-	-
Fresh d-V <sub>2</sub> CT <sub>x</sub> (after Ar etching)	513	32%	514.4	27%	516.4	42%	-	-
d-V <sub>2</sub> CT <sub>x</sub> (after one month)	-	-	515.67	8%	516.69	22%	517.78	70%
Fresh Li-V <sub>2</sub> CT <sub>x</sub>	513.2	30%	514.7	29%	516.7	41%	-	-
Fresh Li-V <sub>2</sub> CT <sub>x</sub> (after Ar etching)	513	36%	514.5	31%	516.7	33%	-	-
Li-V <sub>2</sub> CT <sub>x</sub> (after one month)	513.3	31%	514.5	9%	516.45	60%	-	-

**Figure S4.** V 2p region of the XPS spectra after argon etching. (a) Fresh d-V<sub>2</sub>CT<sub>x</sub>. (b) Fresh Li-V<sub>2</sub>CT<sub>x</sub>.

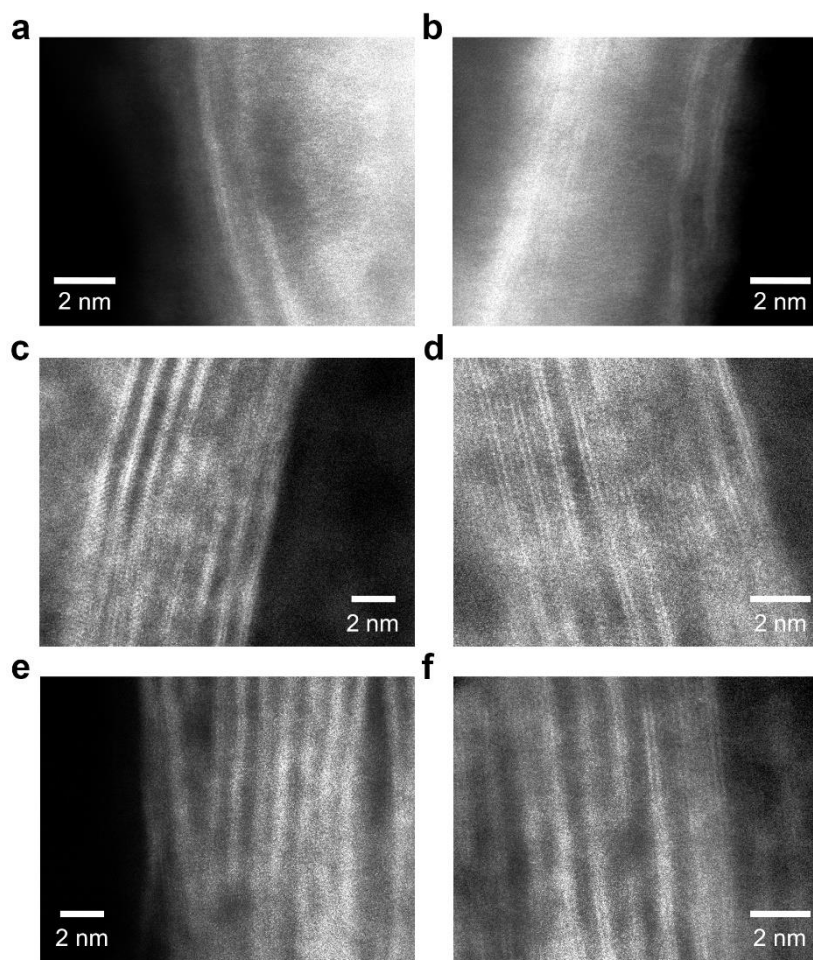


**Figure S5.** STEM images of  $V_2CT_x$  flakes. All TEM samples shown in this figure were prepared by drop casting the MXene solutions on a TEM grid to avoid directional ordering and assembly caused by vacuum filtration and be able to study the stacking and ordering of the flakes before and after cation-assembly. (a and b) STEM images of delaminated  $V_2CT_x$  (d- $V_2CT_x$ ). The stacked (2 to 3) layers observed in the images are most probably due to self-restacking of delaminated flakes during drying on TEM grid. As seen in these images, d- $V_2CT_x$  do not show ordered stacking. It is worth mentioning that d- $V_2CT_x$  flakes were sensitive to the electron beam and at high magnifications their structure was degrading during their observation. Therefore, obtaining higher magnification images was not possible. (c and d) STEM images of Li- $V_2CT_x$  at different magnifications. In a good agreement with XRD results, TEM revealed higher ordering for  $V_2CT_x$  flakes restacked with  $Li^+$  compared to other cations such as  $Na^+$ . The stacking number of flakes was around 8-10 for Li- $V_2CT_x$ . (e and f) STEM images of  $V_2CT_x$  flakes restacked with  $Na^+$  (Na- $V_2CT_x$ ) at different magnifications.  $Na^+$  restacked  $V_2CT_x$  showed less ordering (in good agreement with disappearance of (0006) and (0008) XRD peaks). Based on STEM images, the stacking number of Na- $V_2CT_x$  sample was 10-13.

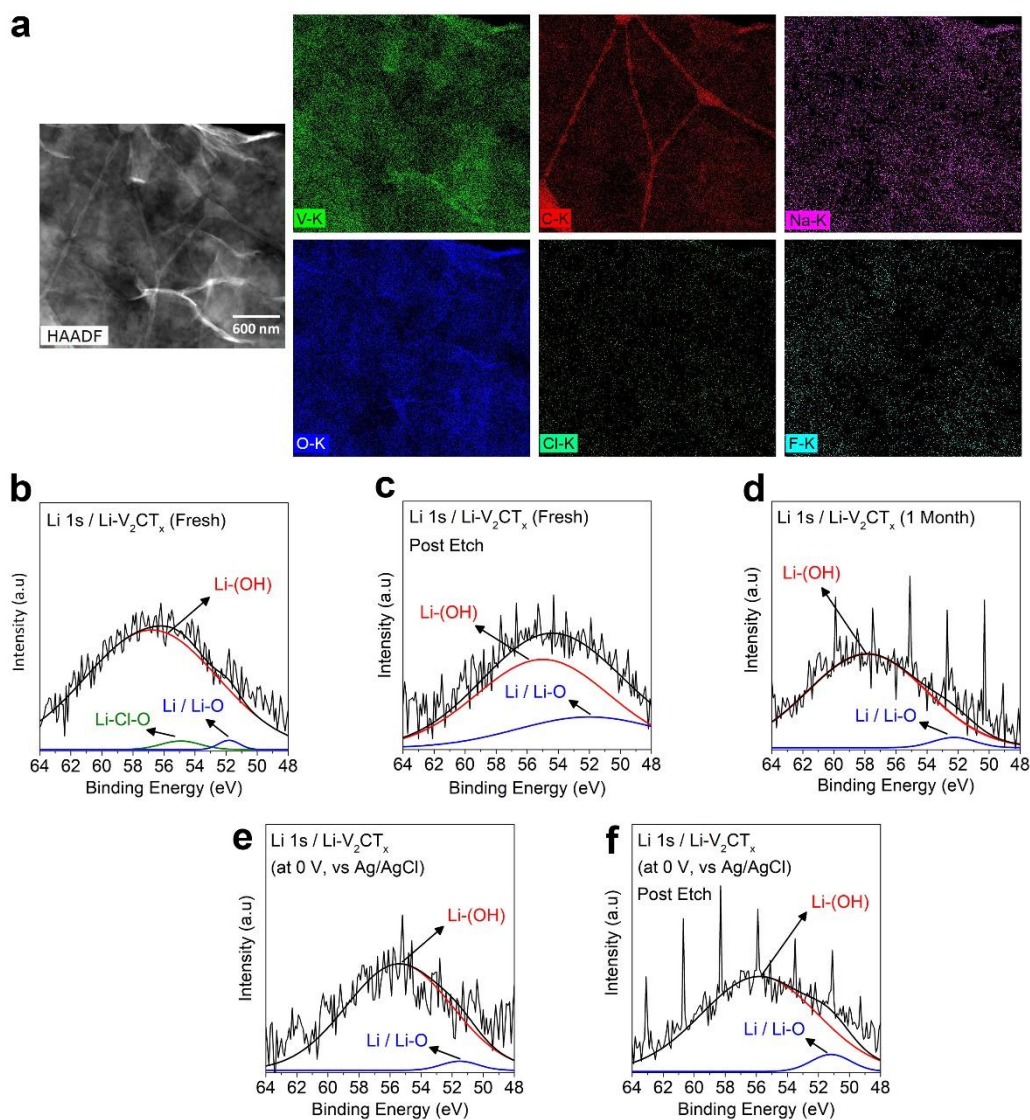


**Figure S6.** EDS and XPS results confirming the presence of Li and Na cations in the  $\text{Li-V}_2\text{CT}_x$  and  $\text{Na-V}_2\text{CT}_x$  flakes. (a) TEM/EDS results of  $\text{Na-V}_2\text{CT}_x$  confirming the presence of sodium in between the layers. (b and c) XPS results for Li 1s region of a  $\text{Li-V}_2\text{CT}_x$  sample, showing the presence of  $\text{Li}^+$  in the sample before and after argon etching, respectively, indicating the presence of Li in the bulk of sample as well as its surface. (d) High-resolution XPS results for Li 1s region of a  $\text{Li-V}_2\text{CT}_x$  sample after one month. (e and f) High-resolution XPS results for Li 1s region of a  $\text{Li-V}_2\text{CT}_x$  sample charged to 0 V (V vs. Ag/AgCl) in 5 M LiCl before and after Argon etching, respectively. The XPS results show that the Li cations, placed in between the layers during the cation-driven assembly synthesis process, are very stable inside the structure and even after electrochemical deintercalation (charging of the electrode) some Li atoms remain in the electrode.

**Table S2.** EDS analysis of different  $V_2CT_x$  samples. EDS analysis of different  $V_2CT_x$  films confirmed the presence of different cations after the assembly process. EDS analysis of  $Li-V_2CT_x$  electrodes after electrochemical cycling in 1 M  $Na_2SO_4$  and 1 M  $MgSO_4$  electrolytes showed the presence of the intercalating cations (cells were opened when electrodes were discharged to lower cut off potential). No Al was detected in any of the delaminated and restacked films, showing complete etching and delamination of  $V_2CT_x$  and absence of any residual MAX phase in the produced films. Carbon contents are not included in the table.

Sample	at. %							
	V	O	F	Li	Na	K	Mg	Al
<b>d-<math>V_2CT_x</math></b>	17.93	22.38	15.73	-	-	-	-	0
<b>Li-<math>V_2CT_x</math></b>	20.47	31.32	11.86	x*	-	-	-	0
<b>Na-<math>V_2CT_x</math></b>	26.25	15.46	19.72	-	2.04	-	-	0
<b>Mg-<math>V_2CT_x</math></b>	23.72	30.52	18.98	-	-	-	3.39	0
<b>Li-<math>V_2CT_x</math> at Lower Cut off potential in <math>MgSO_4</math></b>	35.5	N/A	29.43	x*	-	-	1.43	0
<b>Li-<math>V_2CT_x</math> at Lower Cut off potential in <math>Na_2SO_4</math></b>	34.87	N/A	32.36	x*	4.34	-	-	0

x\*: Not detectable with EDS.

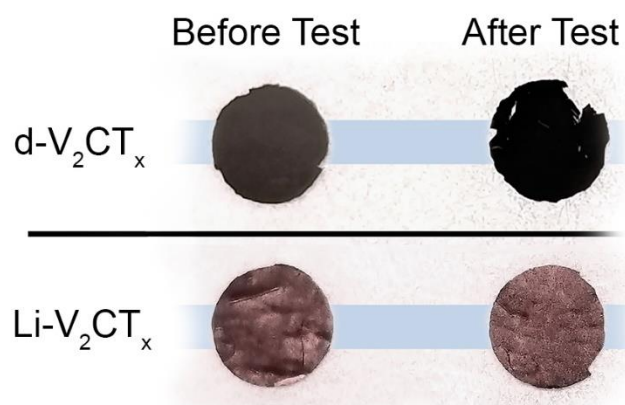


**Figure S7.** Digital photographs of electrodes before and after test. Digital photographs of a freshly delaminated V<sub>2</sub>CT<sub>x</sub> electrode (d-V<sub>2</sub>CT<sub>x</sub>) before and after cycling in a 5 M LiCl electrolyte, showing the change in the color of the electrode and brittleness after the test (the black color after the test is similar to the ambient oxidized V<sub>2</sub>CT<sub>x</sub> film). Digital photographs of a Li-V<sub>2</sub>CT<sub>x</sub> electrode before and after cycling in 5 M LiCl electrolyte, showed no visual change in color or flexibility (in good agreement with electrochemical results).

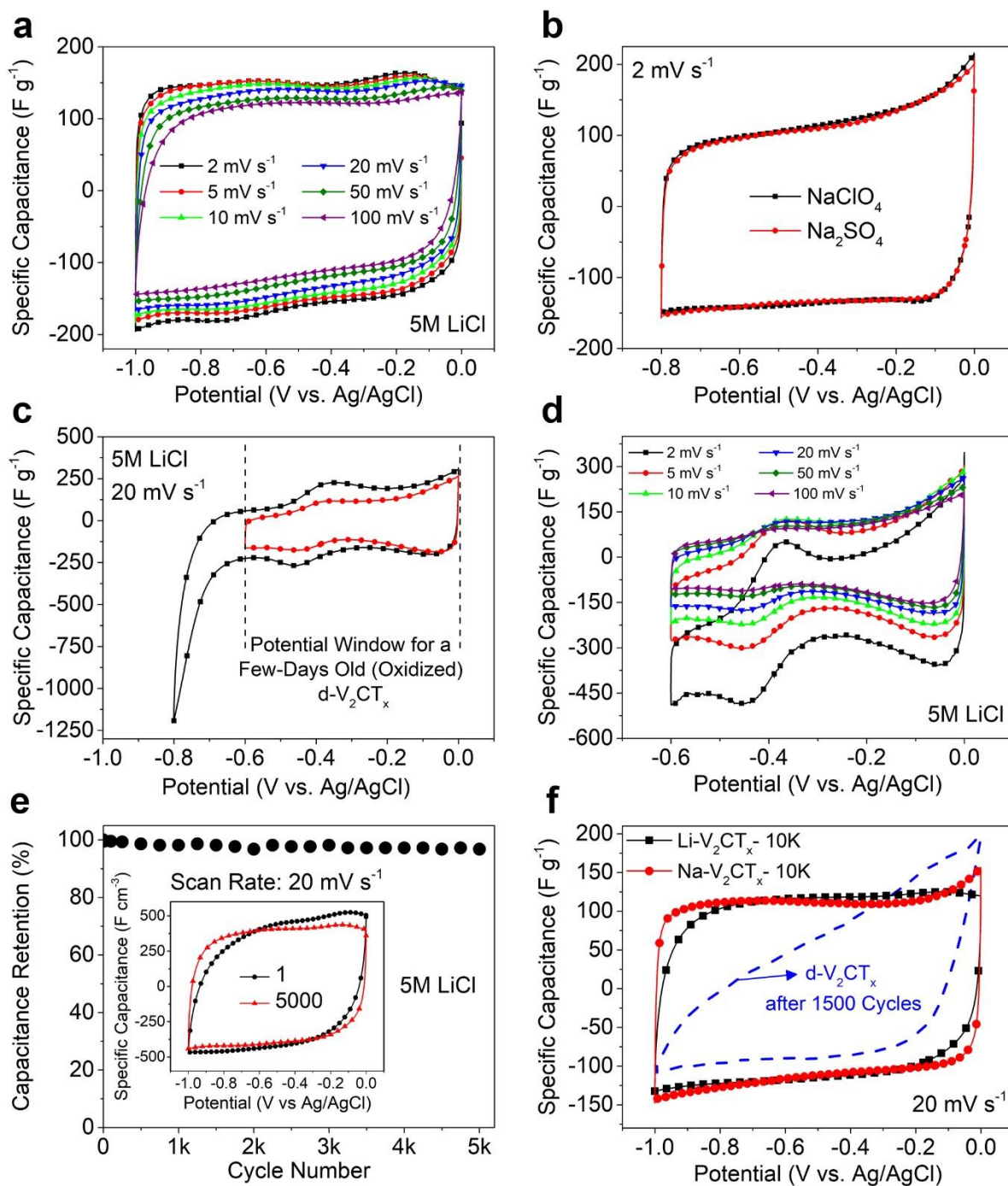


**Figure S8.** Electrochemical behavior of  $\text{V}_2\text{CT}_x$ : cycle life and cation intercalation. (a) CV profiles of  $\text{Na-V}_2\text{CT}_x$  in 5 M LiCl at different scan rates of 2 to 100  $\text{mV s}^{-1}$  showing excellent rate capability and near-rectangular shapes of the CV curves. (b) CV profiles of  $\text{Na-V}_2\text{CT}_x$  in 1 M  $\text{Na}_2\text{SO}_4$  and 1 M  $\text{NaClO}_4$  electrolytes at 2  $\text{mV s}^{-1}$ . The similar shape of CVs as well as comparable capacitance of the electrodes in these electrolytes with different anionic species further confirms the hypothesis that the intercalating ionic species are cations and not anions. (c) CV of a few days old d- $\text{V}_2\text{CT}_x$  (oxidized, similar to the one-week old black film in Fig 1d of the main article). The oxidized films showed a much narrower potential window (0.6 V) compared to the freshly synthesized films (1V, similar to cation-assembled films). A long tail was observed in the CV at potentials lower than -0.6 V. (d) CVs

of the oxidized d- $V_2CT_x$  film at scan rates of  $2\text{ mV s}^{-1}$  to  $100\text{ mV s}^{-1}$  showing a large irreversibility in the CV curves. (e) Cyclic performance of a  $4\text{ }\mu\text{m}$  thick Li- $V_2CT_x$  electrode at a scan rate of  $20\text{ mV s}^{-1}$  in  $5\text{ M LiCl}$  with no sign of degradation or capacitance loss after 5,000 cycles. (f) CVs of Li- $V_2CT_x$  and Na- $V_2CT_x$  electrodes at a scan rate of  $20\text{ mV s}^{-1}$  after 10,000 cycles in  $5\text{ M LiCl}$ . The assembled  $V_2CT_x$  electrodes maintained their rectangular capacitive CV shape even after long cycling and showed superior stability and cycle life compared to d- $V_2CT_x$  electrodes (shown by the dashed line), which drastically lost their capacitance in less than 1,500 cycles.

**Further explanation of charge storage mechanism:** As discussed in the main text of the paper, based on the electrochemical analysis of the electrodes, we suggest that similar to  $Ti_3C_2T_x$ , the charge storage mechanism for  $V_2CT_x$  MXene is intercalation based pseudocapacitance. As shown in Figure S20, the fabricated electrodes have a relatively low surface area compared to activated carbon and other high surface area materials used as EDLC electrodes. Therefore, as previously shown in the case of  $Ti_3C_2T_x$ , the observed high capacitance is mainly related to fast redox reactions that follow the intercalation of ions between MXene layers and are accompanied by the change in the oxidation state of MXene's transition metal.<sup>[18–20]</sup> Previously, the high pseudocapacitance of  $Ti_3C_2T_x$  in  $3\text{ M H}_2\text{SO}_4$  has been ascribed to intercalation of protons and change in the oxidation state of Ti, where this change was accompanied by protonation of the oxygen functional groups on the surface of MXene layers.<sup>[18,21,22]</sup>  $V_2CT_x$  MXene has very similar surface chemistry to that of  $Ti_3C_2T_x$ <sup>[11,23,24]</sup> and its electrochemical behavior in many electrolytes (e. g., CV curves for the tests performed in  $3\text{ M H}_2\text{SO}_4$  electrolyte shown in Figure 5a) are similar to the general electrochemical behavior of  $Ti_3C_2T_x$  with broad and distinct redox couples. We have clearly observed the intercalation of electrolyte ions into between MXene layers in XRD experiments (shown in Figure S15), where change in the interlayer spacing was observed after ion intercalation. Ion intercalation is slower at the beginning of the charge-discharge process, but accessibility of the electrode interlayer spacing increases as the intercalation process continues. As a result, in some electrolytes (particularly those with larger and higher charge density cations) we observe a gradual increase in the capacitance and expansion of the area under CV curves during cycling (further explained in Figure S9 below). This behavior has been previously reported for other MXenes and together with XRD and electrochemical results discussed above confirm a charge storage mechanism based on intercalation pseudocapacitance.<sup>[18,19,22]</sup>

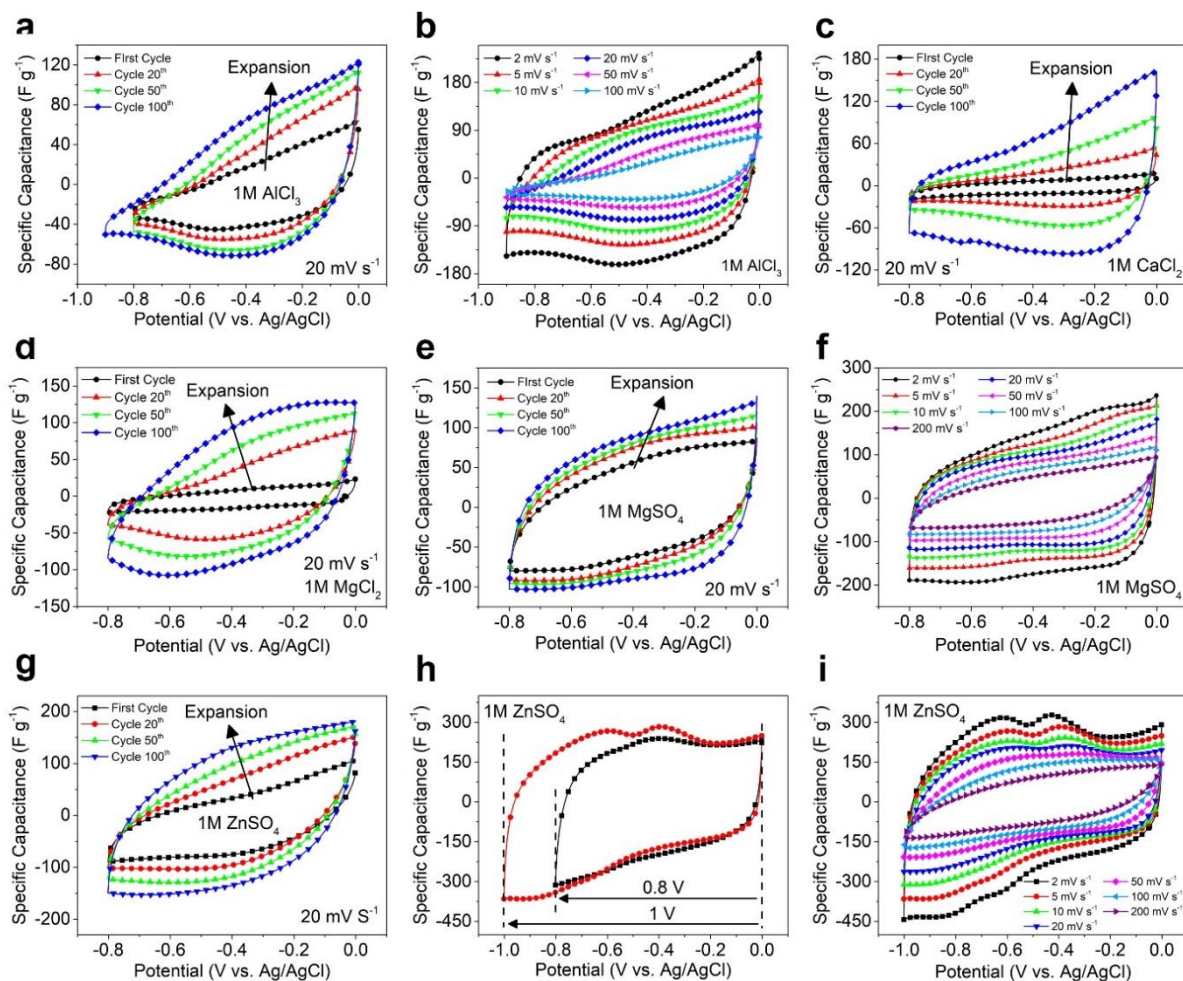


**Figure S9.** Increase in CV current of Na-V<sub>2</sub>CT<sub>x</sub> electrodes during initial cycling in different electrolytes. (a) Increase in CV currents and the expansion of areas under CV curves during the first 100 cycles in AlCl<sub>3</sub> electrolyte. (b) CVs of Na-V<sub>2</sub>CT<sub>x</sub> in AlCl<sub>3</sub> at scan rates from 2 mV s<sup>-1</sup> to 100 mV s<sup>-1</sup>. (c) Expansion of CV area during the first 100 cycles in CaCl<sub>2</sub> electrolyte. (d and e) Initial CVs in 1 M MgCl<sub>2</sub> and 1 M MgSO<sub>4</sub> electrolytes showing the expansion of CV area upon intercalation of Mg<sup>2+</sup> during the first 100 cycles. (f) CVs in 1 M MgSO<sub>4</sub> electrolyte at scan rate ranging from 2 mVs<sup>-1</sup> to 200 mV s<sup>-1</sup>. (g) Initial expansion of CV in ZnSO<sub>4</sub> electrolyte upon Zn<sup>2+</sup> intercalation. (h) CVs in ZnSO<sub>4</sub> in two different lower cut-off potentials at scan rate of 5 mV s<sup>-1</sup>. By increasing the lower potential to -1 V, another pair of oxidation (-0.7 V) and reduction (-0.85 V) peaks was observed. (i) CVs in 1 M ZnSO<sub>4</sub> electrolyte at scan rates of 2 mV s<sup>-1</sup> to 200 mV s<sup>-1</sup>.

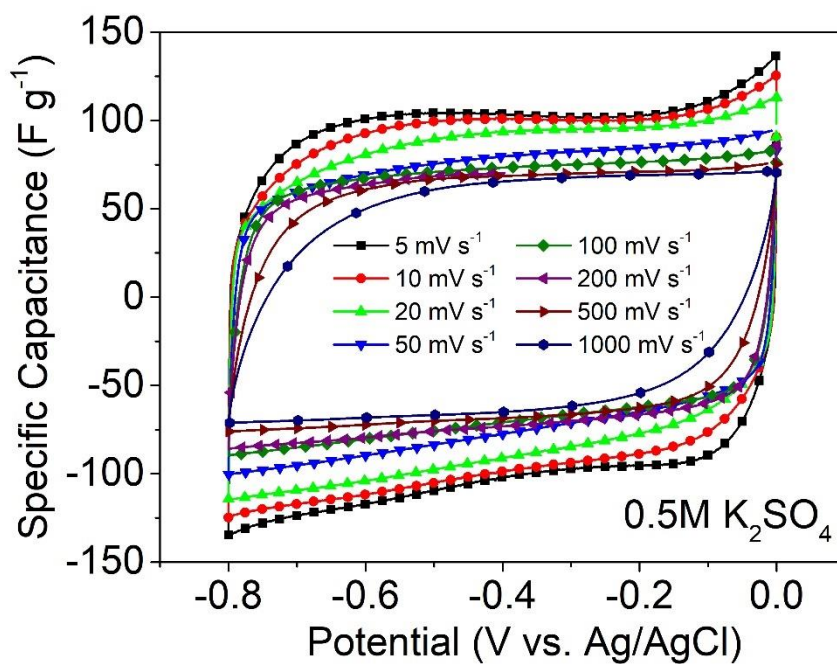


**Figure S10.** CV profiles of a Na-V<sub>2</sub>CT<sub>x</sub> electrode in 0.5 M K<sub>2</sub>SO<sub>4</sub> electrolyte at scan rates ranging from 5 mV s<sup>-1</sup> to 1000 mV s<sup>-1</sup>. The CV curves remained near-rectangular in all scan rates demonstrating the excellent rate capability of the assembled V<sub>2</sub>CT<sub>x</sub> MXene electrodes.

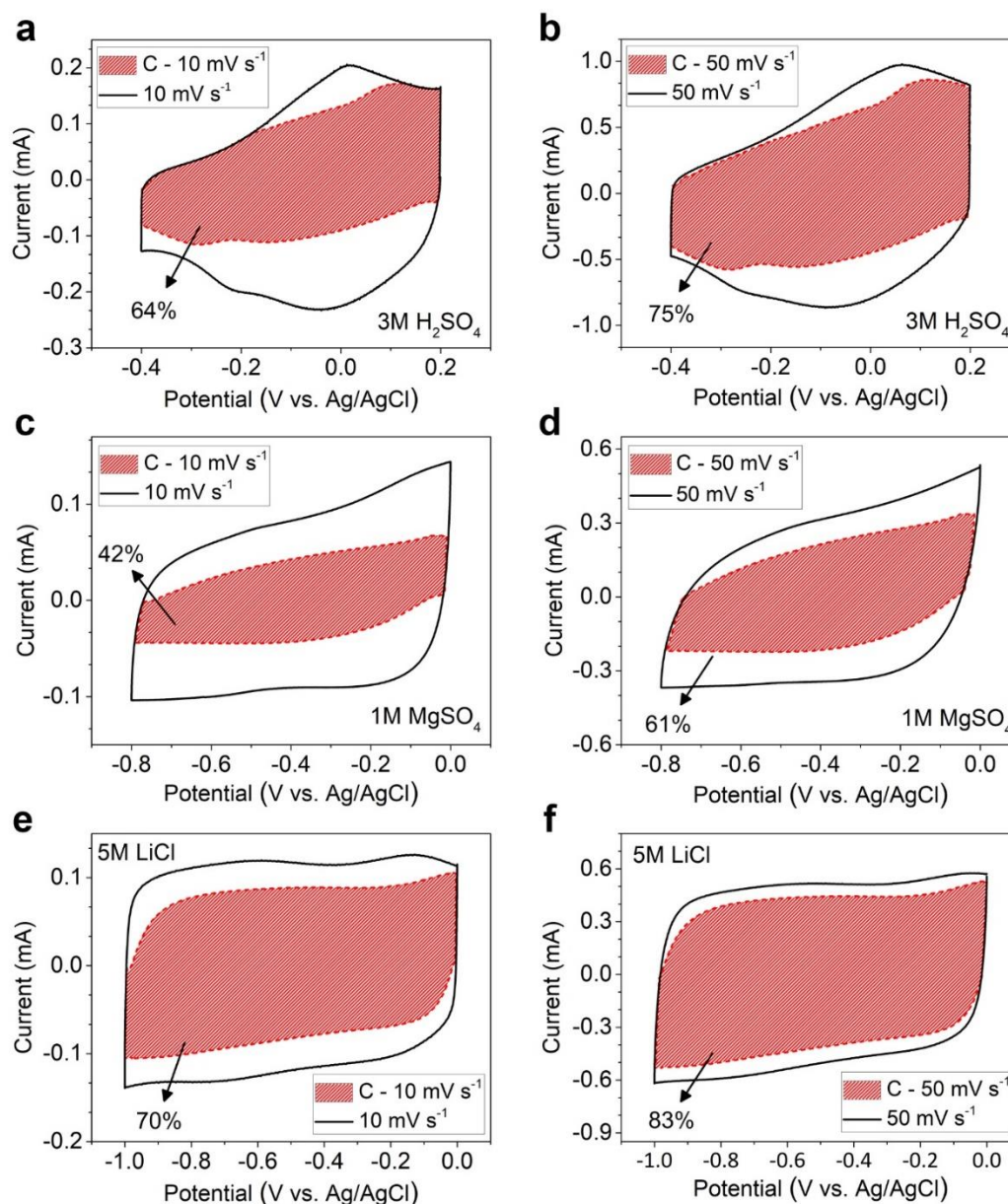


**Figure S11.** Analysis of the charge storage mechanism of Na-V<sub>2</sub>CT<sub>x</sub> electrodes in various electrolytes at two scan rates of 10 mV s<sup>-1</sup> and 50 mV s<sup>-1</sup>. The hatched portions of the graphs show charge storage based on surface-controlled reactions (fast redox) and the remaining portion of the CVs indicate diffusion-controlled reactions (intercalation and Faradic reactions). (a and b) Charge storage mechanism in 3 M H<sub>2</sub>SO<sub>4</sub> showing mostly pseudocapacitive charge storage with a higher contribution from Faradic reactions at lower scan rates. (c and d) Charge storage mechanism in 1 M MgSO<sub>4</sub> showing mostly a diffusion-controlled mechanism (due to sluggish and slow intercalation of Mg<sup>2+</sup>), in good agreement with the gradual expansion of the CV in a MgSO<sub>4</sub> electrolyte. (e and f) Charge storage mechanism in 5 M LiCl electrolyte. The smaller size of the Li<sup>+</sup> cations results in a more facile intercalation and a better accessibility of electrolyte's ions to the MXene surface for redox reactions. Surface-controlled reactions have therefore a higher contribution in Li-based electrolytes.

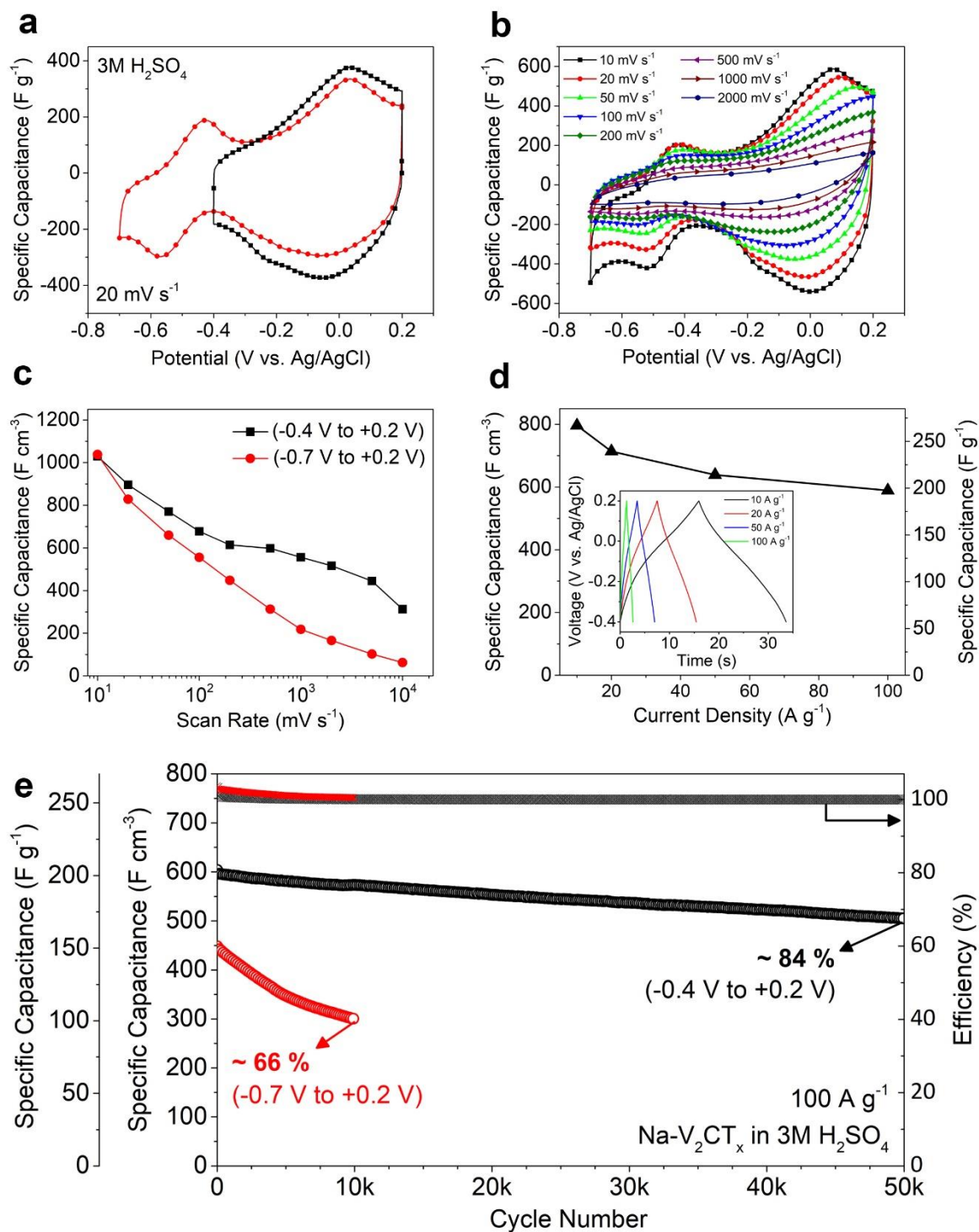


**Figure S12.** Potential window and cycle life performance of Na-V<sub>2</sub>CT<sub>x</sub> electrode in 3 M H<sub>2</sub>SO<sub>4</sub>. (a) CVs of Na-V<sub>2</sub>CT<sub>x</sub> in two different potential windows in 3 M H<sub>2</sub>SO<sub>4</sub> electrolyte. Increasing the lower cut off potential resulted in appearance of another redox pair with wider peak separation potentials and less reversibility. We believe these second redox peaks are due to an irreversible reaction of the MXene with the acidic electrolyte, which causes a rapid decay in the performance of the cell over cycling as well as at higher scan rates.<sup>[25]</sup> (b) CV profiles of Na-V<sub>2</sub>CT<sub>x</sub> at scan rates of 10 mV s<sup>-1</sup> to 2000 mV s<sup>-1</sup> in the larger potential window, showing rapid capacity decay at higher scan rates. (c) Rate performance of Na-V<sub>2</sub>CT<sub>x</sub> electrode in narrow and wide potential windows. (d) Rate capability of Na-

$V_2CT_x$  in 3 M  $H_2SO_4$  at charge-discharge rates from 10 to 100  $A\ g^{-1}$ . Inset shows charge-discharge (voltage vs. time) profiles. (e) Cycle life performance of Na- $V_2CT_x$  electrode at 100  $A\ g^{-1}$  in the narrow and wide potential windows. The electrode could withstand  $\sim 84\%$  of the initial capacitance after 50,000 cycles in the narrow potential window while in the wider potential window the capacitance dropped to  $\sim 66\%$  of the initial capacitance just after 10,000 cycles. It is important to note that in the  $H_2SO_4$  electrolyte, unlike other tested electrolytes, the Na- $V_2CT_x$  electrodes showed the same high pseudocapacitive response from the initial cycles. This is due to the significantly smaller size of protons compared to alkali cations and their fast intercalation between MXene layers.<sup>[2,18]</sup>

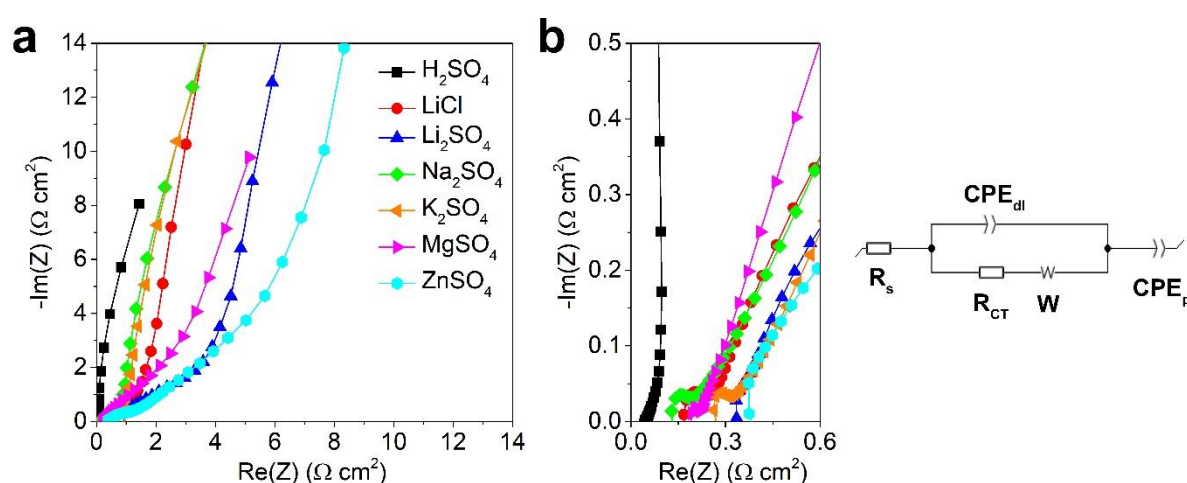


**Figure S13.** The results of electrochemical impedance spectroscopy (EIS) measurements of Na- $V_2CT_x$  film electrodes. (a) Low-frequency region for Nyquist plots of the electrodes in various electrolytes (measurements were performed at OCV and for the frequency range of 100 mHz to 1000 kHz). (b) High-frequency region of the Nyquist plots shown in (a) as well as the equivalent circuit used to fit the EIS data, where  $R_s$  is the bulk electrolyte resistance,  $CPE_{dl}$  is the double-layer capacitance which usually exists in parallel with  $R_{CT}$ , the charge transfer resistance, and  $W$ , a Warburg diffusion element<sup>[26,27]</sup>, and  $CPE_p$  is the pseudocapacitance element.<sup>[28,29]</sup> EIS results showed the capacitive performance of the electrodes in all electrolytes. However, for  $H_2SO_4$  electrolyte the shape of the Nyquist plot is very close to an ideal capacitive response, with a short length of 45-degree linear part (Warburg impedance related to the ion transport resistance in the electrodes), and an almost vertically rising imaginary impedance at low frequencies.<sup>[18]</sup> The EIS data show that ion transport resistance in salt solutions is higher than in  $H_2SO_4$  electrolyte. This is in line with our conclusions derived from CV tests, which reveal slower intercalation of alkali cations as compared to protons. For the electrodes tested in salt electrolytes, small semi-circles are observed in the low-frequency region of Nyquist plots. This is believed to stem from charge-transfer resistance arising from removal or rearrangement of the cation hydration shell during intercalation.<sup>[30,31]</sup>

**Table S3.** Calculated values for  $R_s$  (bulk electrolyte resistance),  $R_{CT}$  (charge transfer resistance),  $CPE_{dl}$ , (double-layer capacitance, and  $CPE_p$  (pseudocapacitance) elements in the equivalent circuit of the EIS data shown in Figure S13.

	$R_s$ (ohm $cm^2$ )	$R_{ct}$ (ohm $cm^2$ )	$CPE_{dl}$ ( $F s^{(a-1)}$ )	$CPE_p$ ( $F s^{(a-1)}$ )
$H_2SO_4$	0.045	0.07	$9 \times 10^{-3}$	0.018
$LiCl$	0.167	1.43	$5.4 \times 10^{-3}$	0.014
$Li_2SO_4$	0.386	1.902	$3.98 \times 10^{-3}$	0.0124
$Na_2SO_4$	0.112	0.884	$5.1 \times 10^{-3}$	0.034
$K_2SO_4$	0.269	1.407	$4.96 \times 10^{-3}$	0.03
$Mg_2SO_4$	0.214	2.099	$4.25 \times 10^{-3}$	0.0231
$ZnSO_4$	0.279	2.275	$2.33 \times 10^{-3}$	0.0197

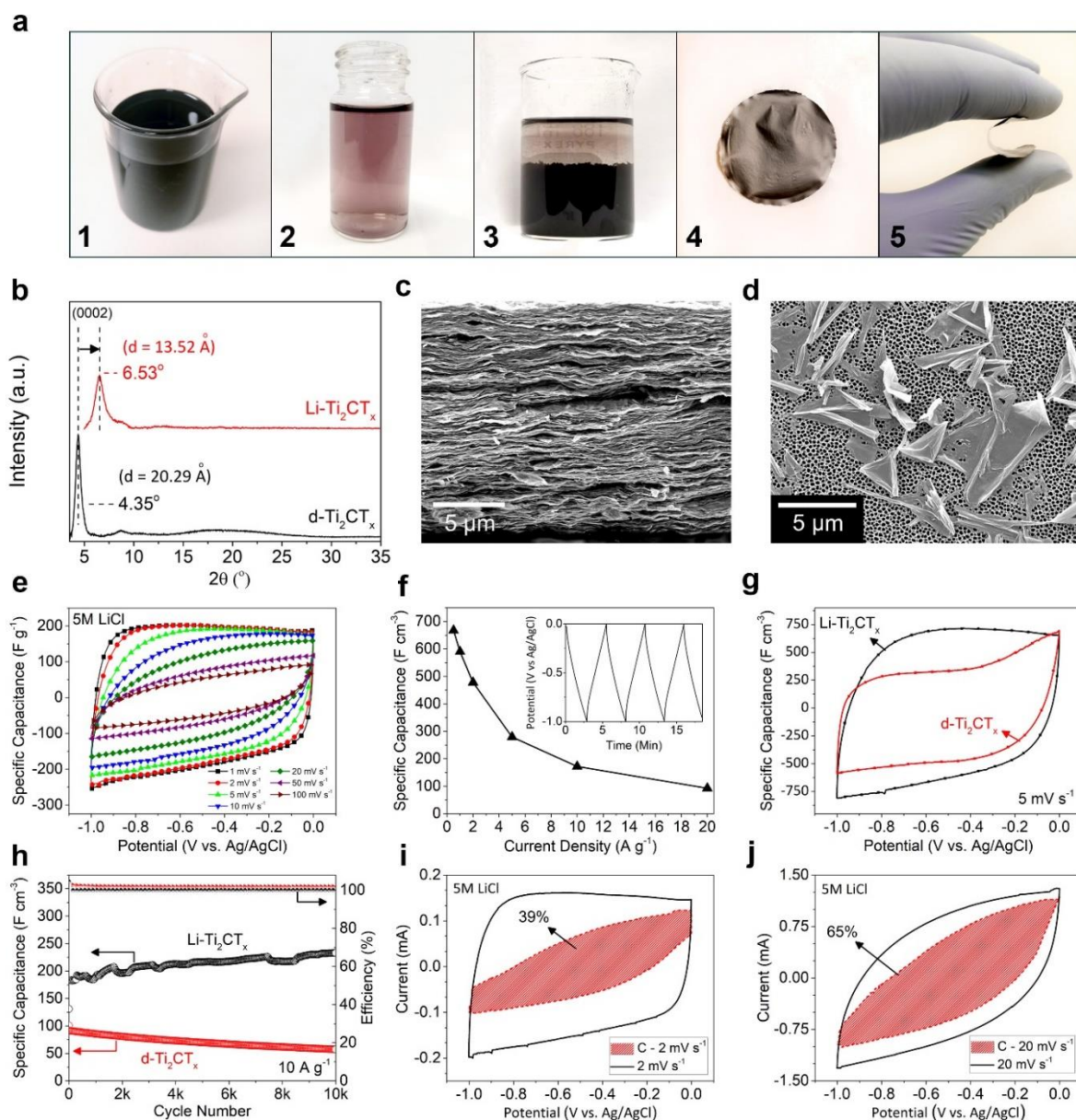


**Figure S14.** Cation-assisted assembly and electrochemical performance of  $\text{Ti}_2\text{CT}_x$  flakes. (a 1-6), Photographs of delaminated (concentrated)  $\text{d-Ti}_2\text{CT}_x$  dispersion, diluted  $\text{d-Ti}_2\text{CT}_x$  dispersion showing a dark red color, assembly of  $\text{d-Ti}_2\text{CT}_x$  with  $\text{Li}^+$  cations, the corresponding  $\text{Li-Ti}_2\text{CT}_x$  film produced with vacuum filtration, and photograph showing the flexibility of the produced film, respectively. (b) XRD patterns of the  $\text{d-Ti}_2\text{CT}_x$  and  $\text{Li-Ti}_2\text{CT}_x$  films showing the shift of (0002) MXene peak to higher angles for the  $\text{Li-Ti}_2\text{CT}_x$  film. (c) SEM image from the cross-section of the produced  $\text{Li-Ti}_2\text{CT}_x$ . (d) SEM image of the  $\text{Li-Ti}_2\text{CT}_x$  flakes on an alumina membrane. The flake wrinkling happens during drying on AAO membranes. (e) CVs of the  $\text{Li-Ti}_2\text{CT}_x$  electrode at different scan rates in 5 M LiCl electrolyte. (f) Rate capability of the  $\text{Li-Ti}_2\text{CT}_x$  electrode at different current densities. It should be noted that the produced film had a thickness of  $\sim 16 \mu\text{m}$  and the capacitance drop at higher rates can be due to the relatively high thickness of the film as also shown for  $\text{Li-V}_2\text{CT}_x$  films in Supplementary Fig. 16. Inset shows the charge-discharge profiles of the  $\text{Li-Ti}_2\text{CT}_x$  in a 1V potential window. (g) CVs

of the  $\text{Li-Ti}_2\text{CT}_x$  and  $\text{d-Ti}_2\text{CT}_x$  electrodes at scan rate of  $5 \text{ mV s}^{-1}$ . The  $\text{Li-Ti}_2\text{CT}_x$  electrode shows a more rectangular CV curve and a higher capacitance compared to the delaminated  $\text{d-Ti}_2\text{CT}_x$  electrode. These results are in good agreement with the effect of assembly on the electrochemical performance  $\text{V}_2\text{CT}_x$  flakes. (h) Cycle life performance of  $\text{d-Ti}_2\text{CT}_x$  and  $\text{Li-Ti}_2\text{CT}_x$  electrodes at  $10 \text{ A g}^{-1}$ . Similar to our results on  $\text{V}_2\text{CT}_x$  MXene, the performance of the  $\text{d-Ti}_2\text{CT}_x$  film degraded over cycling and its capacitance reached half of its initial value. However, the capacitance of the  $\text{Li-Ti}_2\text{CT}_x$  increased over cycling. We speculate the increase in the capacity over cycling is due to the improved accessibility of cations to deeper intercalations sites inside the thick freestanding electrode. (i and j) Charge storage contributions from surface and diffusion-controlled mechanisms for the  $\text{Li-Ti}_2\text{CT}_x$  electrode at two scan rate of  $2 \text{ mV s}^{-1}$  and  $20 \text{ mV s}^{-1}$ . The charge storage mechanism analyses further confirm the dependence of the capacitance on diffusion-controlled (intercalation) processes.

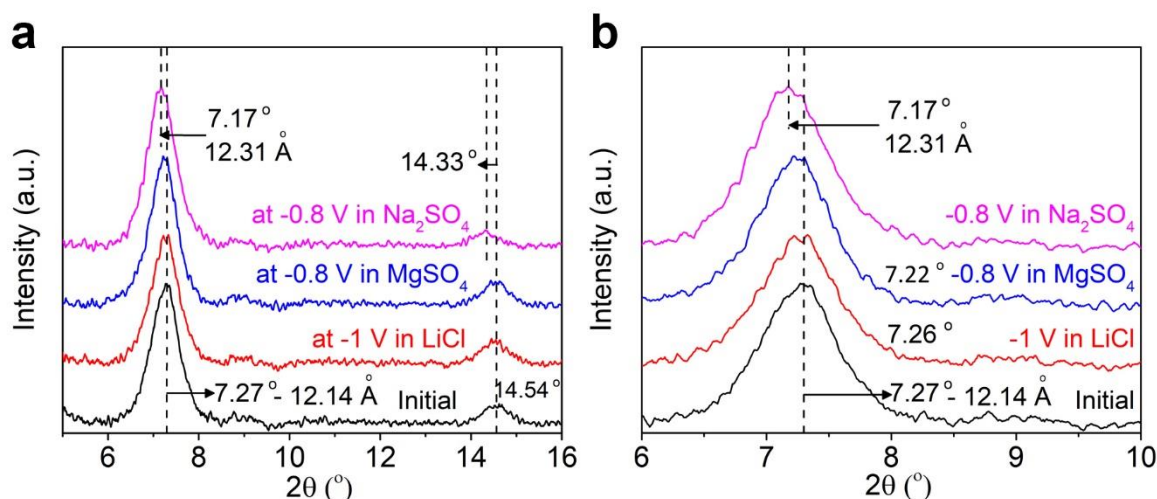


**Figure S15.** *Ex situ* XRD analysis of  $\text{Li-V}_2\text{CT}_x$  electrode after electrochemical intercalation of various cations. (a) Shift of the peak related to the (0002) plane of  $\text{Li-V}_2\text{CT}_x$  electrodes after electrochemical intercalation of various cations. The electrodes were taken off the cells at the end of reduction portion of CV. The electrochemical intercalation of  $\text{Mg}^{2+}$  and  $\text{Na}^+$  cations into  $\text{Li-V}_2\text{CT}_x$  (with initial d-spacing of  $12.14 \text{ \AA}$ ) resulted in a downshift in the position of (0002) peak toward lower angles corresponding to  $0.09 \text{ \AA}$  and  $0.18 \text{ \AA}$  increase in the d-spacing of MXene, respectively. Intercalation of  $\text{Na}^+$  cations also resulted in downshift and broadening of the XRD peak for (0004) planes of MXenes which is in a good agreement with XRD data in Figure S2 for the  $\text{Na}^+$  assembled MXene films. (b) Enlarged version of XRD pattern between 6 and 10 degrees.

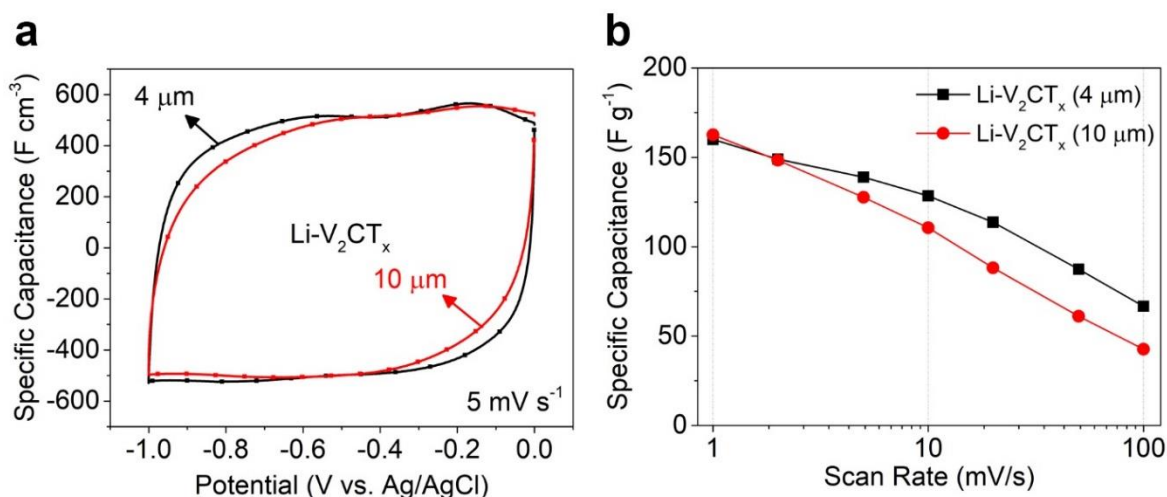


**Figure S16.** Effect of electrode thickness on electrochemical performance. The electrochemical performance of the freestanding films fabricated using 2D materials is often highly dependent on the thickness of the electrodes. The thickness dependent behavior has been previously observed for Ti<sub>3</sub>C<sub>2</sub>T<sub>x</sub> MXene and other 2D materials used as electrodes in ECs.<sup>[2,32]</sup> A severe drop in performance with increasing the thickness can make the electrode useless for practical applications. However, for assembled V<sub>2</sub>CT<sub>x</sub>, the drop in the performance with increasing thickness is very mild. (a) CV curves of a 4 μm and 10 μm thick Li-V<sub>2</sub>CT<sub>x</sub> electrodes at 5 mV s<sup>-1</sup> in 5 M LiCl, showing very small change in the CV curve with increasing the thickness. (b) Comparison of the gravimetric capacitances of the 4 μm and 10 μm thick electrodes at different scan rates, showing the capacitance drop for the thicker electrode at higher scan rates. The diffusion (intercalation) of cations inside the thicker electrodes is slower and contributes to the lower capacitance at higher scan rates.

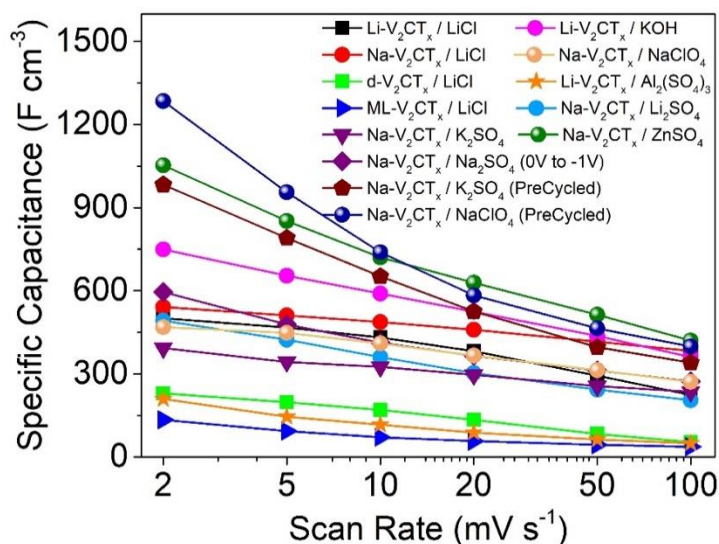


**Figure S17.** Volumetric capacitance of different V<sub>2</sub>CT<sub>x</sub> electrodes in various electrolytes. The term “Pre-cycled” used for some electrodes indicates that those electrodes were cycled over 1,000 cycles to reach their maximum capacitance and were then tested at different rates.

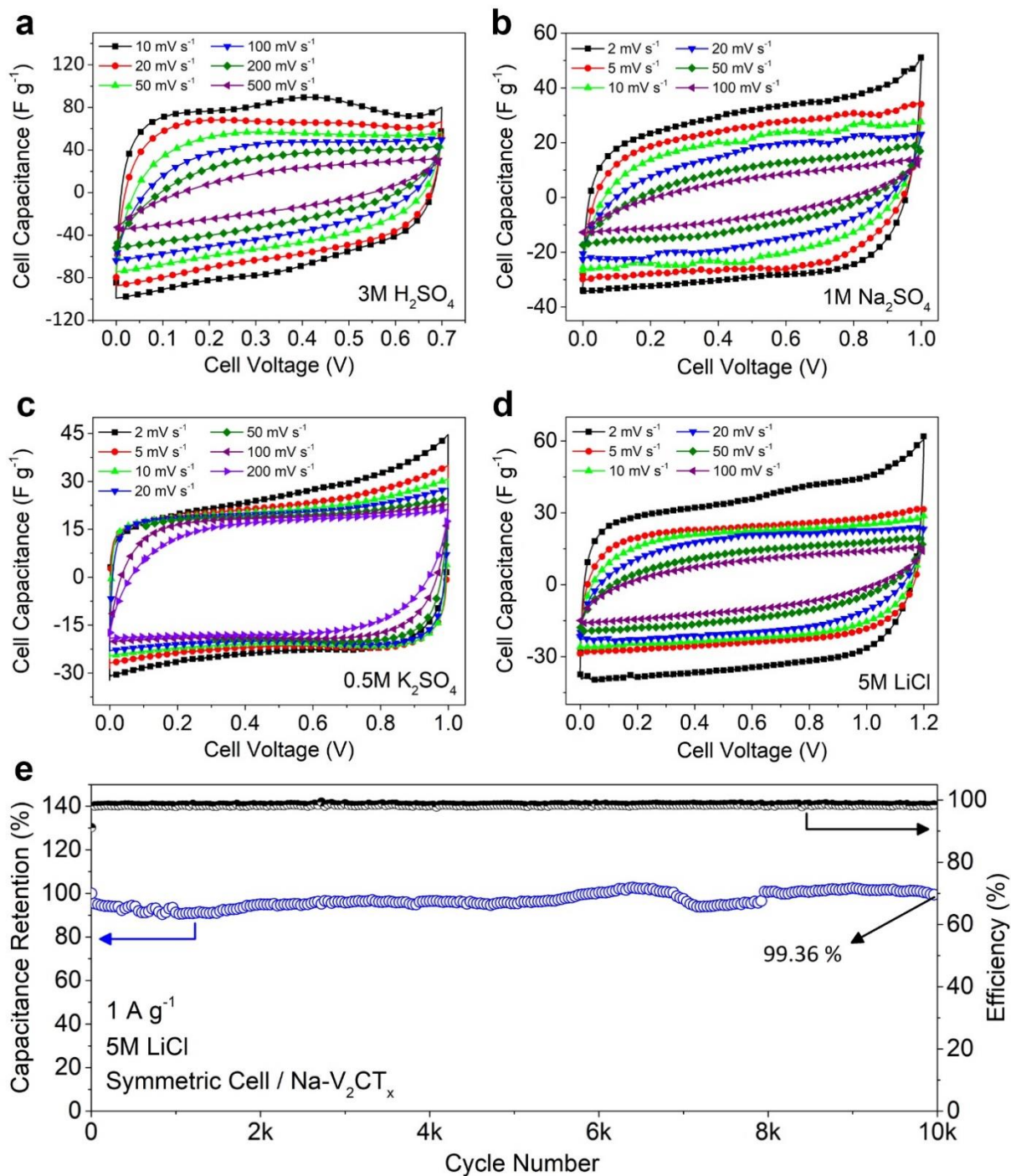


**Figure S18.** CV profiles and cycle performance of symmetric supercapacitors assembled using Na- $V_2CT_x$  electrodes at different scan rates. (a) in 3 M  $H_2SO_4$  electrolyte. (b) in 1 M  $Na_2SO_4$  electrolyte. (c) in 0.5 M  $K_2SO_4$  electrolyte. (d) in 5 M LiCl electrolyte. **e**, Cycle life in 5 M LiCl electrolyte at current density of 1 A  $g^{-1}$  over 10K cycles with a capacitance retention of 99.36%.

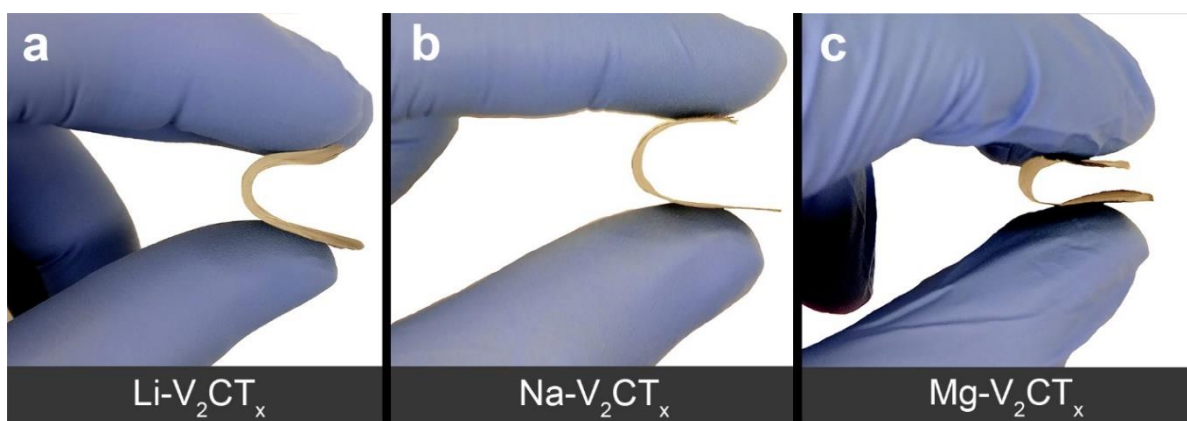


**Figure S19.** Photographs of the films fabricated using assembled C- $V_2CT_x$  flakes showing their flexibility. (a-d) Digital photographs of Li-, Na-, and Mg- $V_2CT_x$  MXene films showing their high flexibility similar to the  $Ti_3C_2T_x$  MXene films.<sup>[2]</sup>

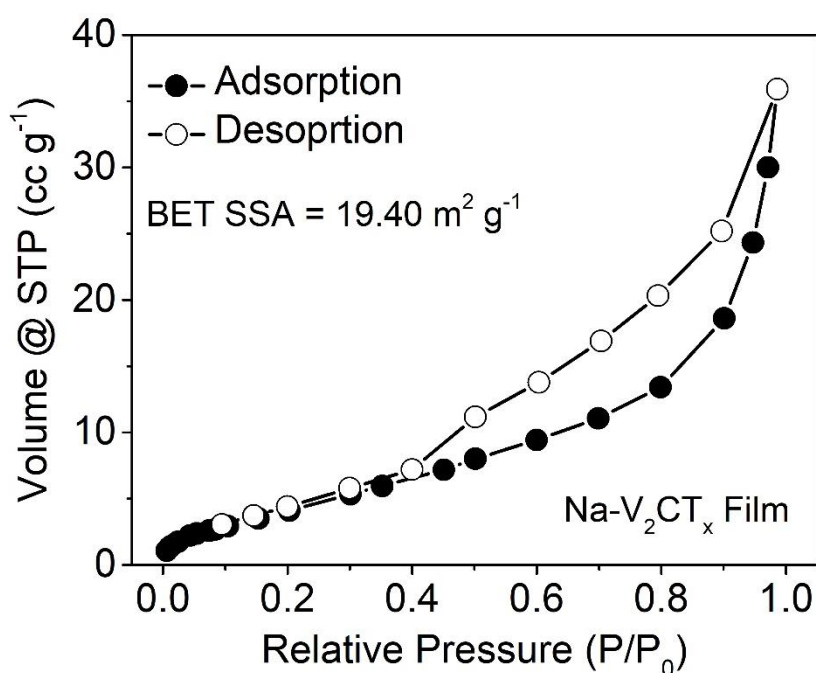


**Figure S20.**  $N_2$  adsorption-desorption isotherms of a Na- $V_2CT_x$  film. The Brunauer-Emmett-Teller (BET) specific surface area (SSA) was measured to be  $19.40\ m^2\ g^{-1}$ . The pore size distribution of the sample was in the range of 10-70 nm in the relative pressure range of 0.4-1.0, and the isotherm suggests that the MXene sample has slit-shaped pores.<sup>[33]</sup>

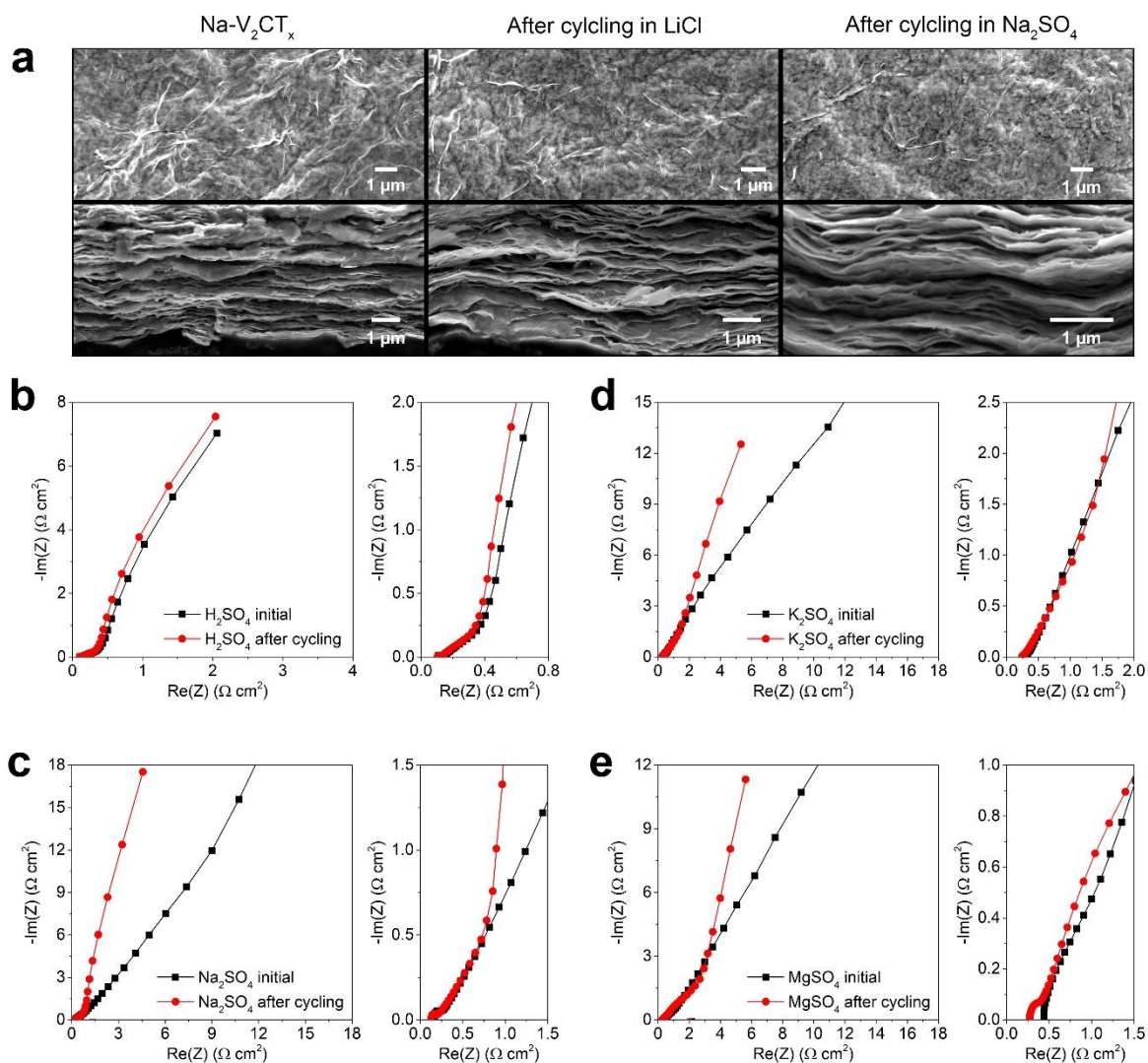


**Figure S21.** (a) SEM images from top-view and cross-section of the Na-V<sub>2</sub>CT<sub>x</sub> films before electrochemical process and after 500 cycles in LiCl and Na<sub>2</sub>SO<sub>4</sub>. Nyquist plots of Na-V<sub>2</sub>CT<sub>x</sub> electrodes in (b) 3 M H<sub>2</sub>SO<sub>4</sub>, (c) 1 M Na<sub>2</sub>SO<sub>4</sub>, (d) 0.5 M K<sub>2</sub>SO<sub>4</sub>, and (e) 1 M MgSO<sub>4</sub> before and after cycling. As it can be seen in this Nyquist plots and in agreement with the results of CV measurements, both ion transport properties and the specific capacitance of the electrodes improve after initial cycles. This is because of the improved electrode wetting and ions accessibility during first several hundred cycles. This effect is more pronounced in case of electrolyte with large cations.

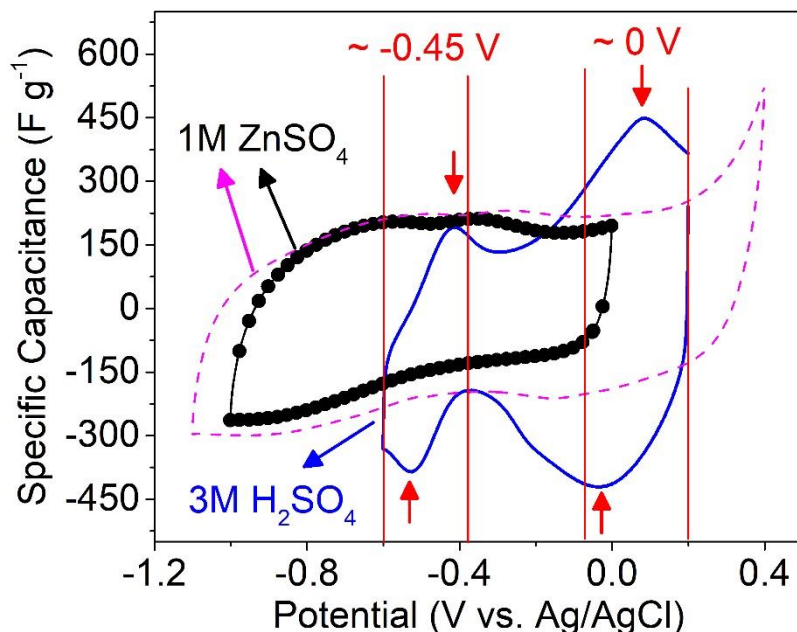


**Figure S22.** Comparison of CVs (at  $20 \text{ mV s}^{-1}$ ) of Na- $\text{V}_2\text{CT}_x$  electrodes in 1 M  $\text{ZnSO}_4$  and 3 M  $\text{H}_2\text{SO}_4$  electrolytes. We use this graph to explain that the higher capacitance of electrodes in 1M  $\text{ZnSO}_4$  electrolyte (pH about 5.4) compared to electrolytes containing  $\text{Li}^+$ ,  $\text{Na}^+$ ,  $\text{K}^+$ ,  $\text{Mg}^{2+}$  is not related to the contribution of  $\text{H}^+$  ions. As it can be seen in this figure, and also shown in Figure 5 and Figure S12,  $\text{V}_2\text{CT}_x$  electrodes show two distinct redox couples centered at around 0 V and -0.45 V when tested in  $\text{H}_2\text{SO}_4$  electrolyte, where  $\text{H}^+$  ions are responsible for the stored charge. As shown by Lukatskaya et al. in case of  $\text{Ti}_3\text{C}_2\text{T}_x$  the redox reactions involve (de)protonation of oxygen functional at the surface of MXene.<sup>[18,22]</sup> We believe that a similar charge storage mechanism is responsible for the high capacitance of  $\text{V}_2\text{CT}_x$  electrodes in the  $\text{H}_2\text{SO}_4$  electrolyte. However, none of these signature redox peaks are observed in the CV curves of  $\text{V}_2\text{CT}_x$  electrodes tested in  $\text{ZnSO}_4$  electrolyte (black CV curves), even when cycled in a large potential window between -1.1 V and 0.4 V, V vs Ag/AgCl (purple dashed CV curve). Therefore, we believe protons have negligible contribution to the high capacitance observed in  $\text{ZnSO}_4$  electrolyte. The higher capacitance of the electrodes in this electrolyte compared to those containing other cations might be related to higher charge of  $\text{Zn}^{2+}$  ions compared to monovalent ions and their smaller size compared to  $\text{Mg}^{2+}$  ions. However, further studies are required to clearly understand the higher capacitance of the MXene electrodes in  $\text{ZnSO}_4$  electrolytes.

## References

- [1] A. Vahidmohammadi, A. Hadjikhani, S. Shahbazmohamadi, M. Beidaghi, *ACS Nano* **2017**, *11*, 11135.
- [2] M. Ghidui, M. R. Lukatskaya, M. Q. Zhao, Y. Gogotsi, M. W. Barsoum, *Nature* **2015**, *516*, 78.
- [3] M. R. Lukatskaya, O. Mashtalir, C. E. Ren, Y. Dall’Agnese, P. Rozier, P. L. Taberna, M. Naguib, P. Simon, M. W. Barsoum, Y. Gogotsi, *Science* **2013**, *341*, 1502.
- [4] V. Augustyn, J. Come, M. a Lowe, J. W. Kim, P.-L. Taberna, S. H. Tolbert, H. D. Abruña, P.

- Simon, B. Dunn, *Nat. Mater.* **2013**, *12*, 518.
- [5] G. Kresse, J. Furthmüller, *Phys. Rev. B - Condens. Matter Mater. Phys.* **1996**, *54*, 11169.
- [6] D. Joubert, *Phys. Rev. B - Condens. Matter Mater. Phys.* **1999**, *59*, 1758.
- [7] P. E. Blöchl, *Phys. Rev. B* **1994**, *50*, 17953.
- [8] J. P. Perdew, K. Burke, M. Ernzerhof, *Phys. Rev. Lett.* **1996**, *77*, 3865.
- [9] J. D. Pack, H. J. Monkhorst, *Phys. Rev. B* **1977**, *16*, 1748.
- [10] B. R. Brooks, C. L. B. III, J. A. D. Mackerell, L. Nilsson, R. J. Petrella, B. Roux, Y. Won, G. Archontis, C. Bartels, S. Boresch, A. Caffisch, L. Caves, Q. Cui, A. R. Dinner, M. Feig, S. Fischer, J. Gao, M. W. I. Hodoscek, M. Karplus, *J. Comput. Chem.* **2009**, *30*, 1545.
- [11] Y. Xie, M. Naguib, V. N. Mochalin, M. W. Barsoum, Y. Gogotsi, X. Yu, K. W. Nam, X. Q. Yang, A. I. Kolesnikov, P. R. C. Kent, *J. Am. Chem. Soc.* **2014**, *136*, 6385.
- [12] Y. Xie, Y. Dall'Agnese, M. Naguib, Y. Gogotsi, M. W. Barsoum, H. L. Zhuang, P. R. C. Kent, *ACS Nano* **2014**, *8*, 9606.
- [13] Y.-X. Yu, *J. Phys. Chem. C* **2016**, *120*, 5288.
- [14] M. Naguib, R. R. Unocic, B. L. Armstrong, J. Nanda, *Dalt. Trans.* **2015**, *44*, 9353.
- [15] S. M. Bak, R. Qiao, W. Yang, S. Lee, X. Yu, B. Anasori, H. Lee, Y. Gogotsi, X. Q. Yang, *Adv. Energy Mater.* **2017**, *7*, 1700959.
- [16] A. Lipatov, M. Alhabeab, M. R. Lukatskaya, A. Boson, Y. Gogotsi, A. Sinitskii, *Adv. Electron. Mater.* **2016**, *2*, 1600255.
- [17] M. Naguib, M. Kurtoglu, V. Presser, J. Lu, J. Niu, M. Heon, L. Hultman, Y. Gogotsi, M. W. Barsoum, *Adv. Mater.* **2011**, *23*, 4248.
- [18] M. R. Lukatskaya, S. Kota, Z. Lin, M. Q. Zhao, N. Shpigel, M. D. Levi, J. Halim, P. L. Taberna, M. W. Barsoum, P. Simon, Y. Gogotsi, *Nat. Energy* **2017**, *6*, 1.
- [19] M. D. Levi, M. R. Lukatskaya, S. Sigalov, M. Beidaghi, N. Shpigel, L. Daikhin, D. Aurbach, M. W. Barsoum, Y. Gogotsi, *Adv. Energy Mater.* **2015**, *5*, 1400815.
- [20] B. Anasori, M. R. Lukatskaya, Y. Gogotsi, *Nat. Rev. Mater.* **2017**, *2*, 16098.
- [21] M. Hu, Z. Li, T. Hu, S. Zhu, C. Zhang, X. Wang, *ACS Nano* **2016**, *10*, 11344.
- [22] M. R. Lukatskaya, S. M. Bak, X. Yu, X. Q. Yang, M. W. Barsoum, Y. Gogotsi, *Adv. Energy Mater.* **2015**, *5*, 1500589.
- [23] M. Naguib, J. Halim, J. Lu, K. M. Cook, L. Hultman, Y. Gogotsi, M. W. Barsoum, *J. Am. Chem. Soc.* **2013**, *135*, 15966.
- [24] K. J. Harris, M. Bugnet, M. Naguib, M. W. Barsoum, G. R. Goward, *J. Phys. Chem. C* **2015**, *119*, 13713.
- [25] X. Lu, M. Yu, T. Zhai, G. Wang, S. Xie, T. Liu, C. Liang, Y. Tong, Y. Li, *Nano Lett.* **2013**, *13*, 2628.
- [26] Y. Y. Horng, Y. C. Lu, Y. K. Hsu, C. C. Chen, L. C. Chen, K. H. Chen, *J. Power Sources* **2010**, *195*, 4418.
- [27] Z. Niu, W. Zhou, J. Chen, G. Feng, H. Li, W. Ma, J. Li, H. Dong, Y. Ren, D. Zhao, S. Xie, *Energy Environ. Sci.* **2011**, *4*, 1440.
- [28] Q. X. Xia, N. M. Shinde, J. M. Yun, T. Zhang, R. S. Mane, S. Mathur, K. H. Kim, *Electrochim. Acta* **2018**, *271*, 351.
- [29] Y. Huang, Y. Li, Z. Hu, G. Wei, J. Guo, J. Liu, *J. Mater. Chem. A* **2013**, *1*, 9809.
- [30] M. Okubo, A. Sugahara, S. Kajiyama, A. Yamada, *Acc. Chem. Res.* **2018**, *51*, 591.

- [31] N. Shpigel, M. D. Levi, S. Sigalov, T. S. Mathis, Y. Gogotsi, D. Aurbach, *J. Am. Chem. Soc.* **2018**, *140*, 8910.
- [32] M. Acerce, D. Voiry, M. Chhowalla, *Nat. Nanotechnol.* **2015**, *10*, 313.
- [33] X. Xie, M. Q. Zhao, B. Anasori, K. Maleski, C. E. Ren, J. Li, B. W. Byles, E. Pomerantseva, G. Wang, Y. Gogotsi, *Nano Energy* **2016**, *26*, 513.